technische universität dortmund

Max-Planck-Institut für molekulare Physiologie

mpi

A protein-based method for the encapsulation of synthetic cytoplasms

Dissertation

Zur Erlangung des akademischen Grades eines Doktors der Naturwissenschaften

(*Dr. rer. nat.*)

Der Fakultät für Chemie und Chemische Biologie

der Technischen Universität Dortmund

Angefertigt am Max-Planck Institut für molekulare Physiologie in Dortmund

Vorgelegt von

Hans Seidel

Dezember 2021

Vorgelegt im Dezember 2021

Von Hans Seidel

Gutachter:

Prof. Dr. Philippe I. H. Bastiaens

Prof. Dr. Hannes Mutschler

The work presented in this thesis was performed in the Department of Systemic Cell Biology lead by Prof. Dr. Philippe I. H. Bastiaens at the Max-Planck Institute of Molecular Physiology, Dortmund, Germany

The work described in this thesis has partly been included in the following publications:

Gavriljuk, K., Scocozza, B., Ghasemalizadeh, F. *et al. A self-organized synthetic morphogenic liposome responds with shape changes to local light cues.* *Nat Commun* **12,** 1548 (2021). https://doi.org/10.1038/s41467-021-21679-2

Eidesstattliche Versicherung (Affidavit)

Name, Vorname
(Surname, first name)

Matrikel-Nr.
(Enrolment number)

Belehrung:

Wer vorsätzlich gegen eine die Täuschung über Prüfungsleistungen betreffende Regelung einer Hochschulprüfungsordnung verstößt, handelt ordnungswidrig. Die Ordnungswidrigkeit kann mit einer Geldbuße von bis zu 50.000,00 € geahndet werden. Zuständige Verwaltungsbehörde für die Verfolgung und Ahndung von Ordnungswidrigkeiten ist der Kanzler/die Kanzlerin der Technischen Universität Dortmund. Im Falle eines mehrfachen oder sonstigen schwerwiegenden Täuschungsversuches kann der Prüfling zudem exmatrikuliert werden, § 63 Abs. 5 Hochschulgesetz NRW.

Die Abgabe einer falschen Versicherung an Eides statt ist strafbar.

Wer vorsätzlich eine falsche Versicherung an Eides statt abgibt, kann mit einer Freiheitsstrafe bis zu drei Jahren oder mit Geldstrafe bestraft werden, § 156 StGB. Die fahrlässige Abgabe einer falschen Versicherung an Eides statt kann mit einer Freiheitsstrafe bis zu einem Jahr oder Geldstrafe bestraft werden, § 161 StGB.

Die oben stehende Belehrung habe ich zur Kenntnis genommen:

Official notification:

Any person who intentionally breaches any regulation of university examination regulations relating to deception in examination performance is acting improperly. This offence can be punished with a fine of up to EUR 50,000.00. The competent administrative authority for the pursuit and prosecution of offences of this type is the chancellor of the TU Dortmund University. In the case of multiple or other serious attempts at deception, the candidate can also be unenrolled, Section 63, paragraph 5 of the Universities Act of North Rhine-Westphalia.

The submission of a false affidavit is punishable.

Any person who intentionally submits a false affidavit can be punished with a prison sentence of up to three years or a fine, Section 156 of the Criminal Code. The negligent submission of a false affidavit can be punished with a prison sentence of up to one year or a fine, Section 161 of the Criminal Code.

I have taken note of the above official notification.

Ort, Datum
(Place, date)

Unterschrift
(Signature)

Titel der Dissertation:
(Title of the thesis):

Ich versichere hiermit an Eides statt, dass ich die vorliegende Dissertation mit dem Titel selbstständig und ohne unzulässige fremde Hilfe angefertigt habe. Ich habe keine anderen als die angegebenen Quellen und Hilfsmittel benutzt sowie wörtliche und sinngemäße Zitate kenntlich gemacht.
Die Arbeit hat in gegenwärtiger oder in einer anderen Fassung weder der TU Dortmund noch einer anderen Hochschule im Zusammenhang mit einer staatlichen oder akademischen Prüfung vorgelegen.

I hereby swear that I have completed the present dissertation independently and without inadmissible external support. I have not used any sources or tools other than those indicated and have identified literal and analogous quotations.

The thesis in its current version or another version has not been presented to the TU Dortmund University or another university in connection with a state or academic examination.*

*Please be aware that solely the German version of the affidavit ("Eidesstattliche Versicherung") for the PhD thesis is the official and legally binding version.

Ort, Datum
(Place, date)

Unterschrift
(Signature)

Contents

I. List of Figures

II. List of Tables

III. List of Abbreviations

+TIP	Plus-end tracking protein
ATP	Adenosine triphosphate
C2lact	C2 domain of lactadherin
cDICE	continuoues Droplet Interface Crossing Encapsulation
CLSM	Confocal laser scanning microscopy
ch-TOG	Colonic and hepatic tumour overexpressed gene protein
COPY^{o}	Atto532-stathmin-Atto647
CRIB	Cdc42/Rac interactive binding
cv	Column volume
Cys	Cysteine
Did2	DOA4-independent degradation protein 2
DOPC	1,2-Dioleoyl-*sn*-glycero-3-phosphocholine
DOPS	1,2-Dioleoyl-*sn*-glycero-3-phosphoserine
EGFP	Enhanced green fluorescent protein
eh	*entamoeba histolytica*
ESCRT	Endosomal sorting complex required for transport
FRET	Förster resonance energy transfer
GDP	Guanosine diphosphate
GGPP	Geranylgeranylpyrophosphate
GGTase I β	Geranylgeranyl transferase 1 β
Gly	Glycine
GTP	Guanosine triphosphate
GUV	Giant unilamellar vesicle
HIV	human immunodeficiency virus
HSE1	Heparanase
iLID	improved Light-inducible Dimer
ILV	Intraluminal vesicle
INCENP	Inner centromere protein
IST1	Increased sodium tolerance protein 1
MAP	microtubule associated protein
MBP	Maltose-binding protein
MLV	Multilamellar vesicle
MT	Microtubule
MTOC	Microtubule organizing centre
MVB	multivesicular bodies
MVV	Multivesicular vesicle
PAK1	p21-activated kinase 1
PE	Phosphatidylethanolamine
PI3P	Phosphatidylinositol 3-phosphate
PPλ	protein phosphatase lambda
RabGGTase β	Rab geranylgeranyl transferase β

Rac1	Ras-related C3 botulinum toxin substrate 1
SEC	Size exclusion chromatography
Ser	Serine
SLAIN2	SLAIN motif-containing protein 2
Snf7	Sucrose nonfermenting protein 7
SspB	Stringent starvation protein B
SUV	Small unilamellar vesicle
synMMS	synthetic Morphogenic Membrane System
TACC3	Transforming acidic coiled-coil-containing protein 3
TOG	tumour overexpressed gene
TPX2	Targeting protein for Xklp2
tRac1	C-terminal domain of Rac1
Vps	Vesicular protein sorting
Xlp2	X-linked lymphoproliferative disease 2

1. Abstract & Zusammenfassung

1.1 Abstract

The generation of a synthetic proto-cell to understand living system proves to be a valuable approach to unravel basic principles of living systems.

In this thesis, an encapsulation method for the generation of small cell-sized proto-cells within giant unilamellar vesicles (GUVs) was developed and the encapsulation method was validated by verifying the functionality of a synthetic morphogenic membrane system (synMMS).

The encapsulation method is inspired by the cellular process of autophagy and conducted by the endosomal sorting complex required for transport (ESCRT). More specifically the encapsulation is archieved by utilizing the scission machinery of ESCRT, ESCRT-III. Target proteins for the encapsulation into intraluminal vesicles (ILVs) are added to the bulk solution around GUVs and the encapsulation is started by adding the subunits of the ESCRT-III machinery to the solution. By this, ILVs are formed within GUVs that are completely separated from the bulk solution. ESCRT-III not only encapsulates target solutions but furthermore inverts the topology of the system from the homogeneous resource unlimited bulk towards the ILV with only a small inhomogeneous reservoir of matter. Uncoupling the systems in this way enables the simultaneous observation of both systems and their interactions with the lipid membranes.

The encapsulation of synMMS without a centralized microtubule cytoskeleton but with a light-induced signalling system connected by the tubulin regulatory protein stathmin revealed fundamental features of the interactions between the signalling and cytoskeletal systems and gives further evidence towards the tubulin nucleation capability of Aurora B kinase.

Thereby, this work represents another step towards the plausible reconstruction of a synthetic autopoietic system.

1.2 Zusammenfassung

Die Generierung einer synthetischen Protozelle zum Verständnis lebender Systeme erweist sich als wertvoller Ansatz zur Entschlüsselung der Grundprinzipien lebender Systeme.

In dieser Arbeit wurde eine Einkapsulierungsmethode zur Erzeugung kleiner zell-großer Protozellen in riesigen unilamellaren Vesikeln (GUVs) entwickelt und die Einkapsulierungsmethode wurde durch den Nachweis der Funktionalität eines synthetischen morphogenen Membransystems (synMMS) bestätigt.

Die Einkapsulierungsmethode ist vom zellulären Prozess der Autophagie inspiriert und wird von dem für den Transport erforderlichen endosomalen Sortierkomplex (ESCRT) durchgeführt. Genauer gesagt wird die Einkapselung unter Verwendung der Spaltungsmaschinerie von ESCRT, ESCRT-III, erzielt. Zielproteine für die Einkapselung in intraluminale Vesikel (ILVs) werden der Lösung um GUVs zugesetzt und die Einkapselung wird durch Zugabe der Untereinheiten der ESCRT-III-Maschinerie zu der Lösung gestartet. Dadurch werden ILVs innerhalb von GUVs gebildet, die vollständig von der Lösung getrennt sind. Dadurch kapselt ESCRT-III nicht nur Ziellösungen ein, sondern invertiert darüber hinaus die Topologie des Systems von der homogenen Ressource unbegrenzter Masse hin zum ILV mit nur einem kleinen inhomogenen Materiereservoir. Die Entkopplung der Systeme auf diese Weise ermöglicht die gleichzeitige Beobachtung beider Systeme und ihrer Wechselwirkungen mit den Lipidmembranen.

Die Einkapselung des synMMS ohne ein zentralisiertes Mikrotubulus-Zytoskelett aber mit einem lichtinduzierten Signalsystem, das durch das Tubulin-regulatorische Protein Stathmin verbunden ist, zeigte grundlegende Merkmale der Interaktion zwischen Signal- und Zytoskelettsystem und liefert weitere Hinweise auf die Tubulin-Nukleationsfähigkeit von Aurora B-Kinase.

Damit stellt diese Arbeit die erfolgreiche Etablierung einer neuen Einkapsulierungsmethode und einen weiteren Schritt zur plausiblen Rekonstruktion eines synthetischen autopoietischen Systems dar.

2. Introduction

2.1 Synthetic biology

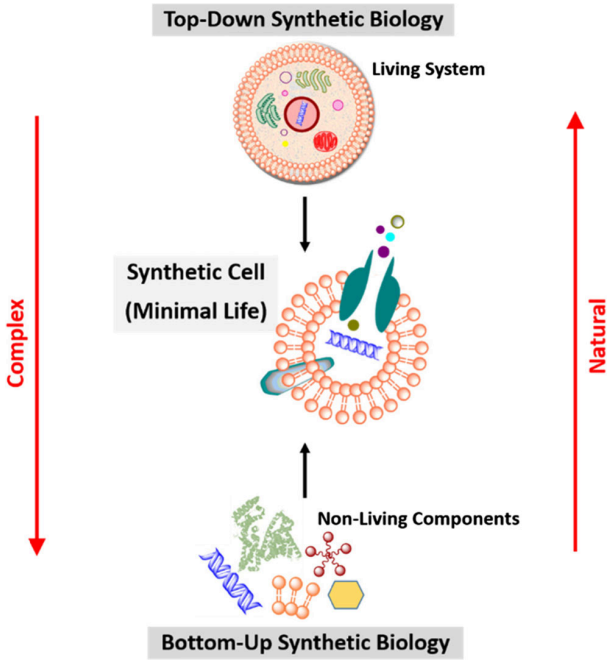

Figure 1 Top-down and bottom-up approach in synthetic biology. Top-down reduces complexity originating from an existing organism. Bottom-up increases complexity from non-living components. Image taken from Damiati 2019[1].

The newly established field of synthetic biology as a synergistic collaboration between engineering, molecular biology and systems biology, aims for the generation of artificial organisms designed by humans[2]. This serves the purpose of understanding what makes a minimal living organism, but furthermore promises enlightenment on how complex the evolutionary process must have been from which life arose.

Within the field emerged two general approaches to generate a minimal living organism, which are bottom-up and top-down[3].

Top-down aims to design a minimal living organism by reducing the complexity of existing organisms to a minimum, whereas bottom-up is aiming to generate it from scratch by building up complexity[4] (Fig. 1). Both approaches require an excellent understanding of cellular and molecular processes to achieve the generation of artificial life.

Additional goals beside understanding the basic principles of life are the generation or modification of organisms for a specific purpose beneficial for humankind. Key points here are the production of competent drugs[5] and counteracting the environmental impact of society[3] (e.g. carbon capture[6]).

2.2 Collective behaviour

To understand the behaviour of a living entity it is not sufficient to observe an isolated component alone. Rather, one has to understand the complexity of the entity and its interactions with its surroundings entities. From these relations arises the collective behaviours found on the different scales of life, from molecular over tissue to social interactions. These interactions lead to a higher scale organization than its single entities would be capable of.

On the organism scale fish form swarms a form of protection from predators[7], and termites build their mounded hives[8].

On the cellular scale, a living system is equipped with complex molecular networks for sensing and actuation, that are capable of complex dynamics. Cells thereby integrate external and internal information and respond accordingly to the stimuli, which can lead to collective cell movement as a response to wounds[9] and other coordinated behaviours such as differentiation, morphogenesis, etc. With this intercellular communication expands the dynamic solutions that the single cell is capable of[10].

2.3 Reconstituted liposomes

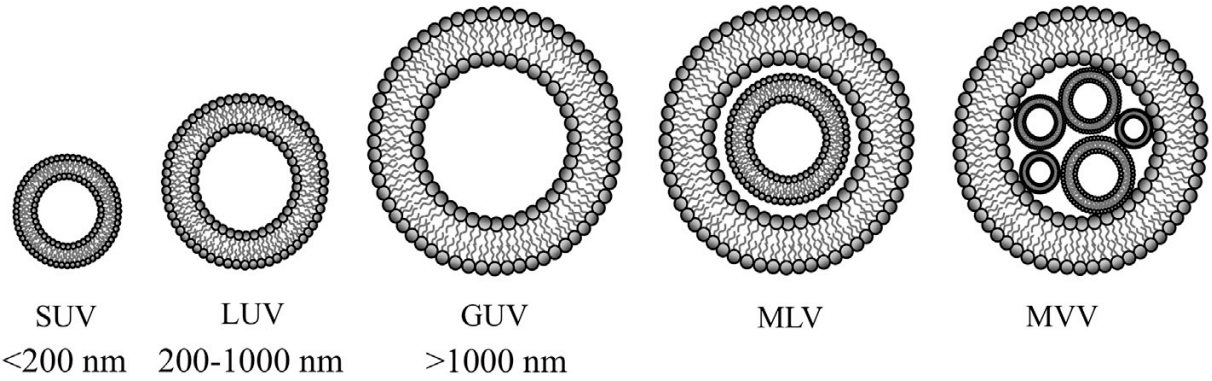

Figure 2 Schematic representation of different liposomes. Small unilamellar Vesicle (SUV), Large unilamellar Vesicle (LUV), Giant unilamellar Vesicle (GUV), Multi-lamellar Vesicle (MLV) and Multi Vesicular Vesicles (MVV). Image taken from Milchvich et. al 2017[11].

The first contact point of a cell to react to external signals, e.g. growth hormones, is the cell membrane. Most signalling networks include proteins located to the membrane, be it transmembrane or peripheral proteins. The membrane further serves as a boundary that separates the internal from the external bulk. These points, makes membranes and membrane systems a crucial part of life, hence the investigation of membrane systems has

taken a central role within synthetic biology and other fields. Methods to generate liposomes for research and medical applications were developed and are improved constantly[12].

Liposomes can vary largely in size depending on the method used and application desired[13,14]. Reconstituted liposomes are therefore classified by size as well as number of internal membranes (Fig. 2). Most interesting for the reconstitution of life-like systems are giant unilamellar vesicles (GUVs) with dimensions of existing organisms[15].

Plenty of methods for the generation of liposomes have been developed over the past decades ranging from the simpler electroformation[16] and double emulsion[17] to more complex ones like micro-fluidic jetting[18]. The lipid compositions used for these methods are simplified and in no form as complex and unique as the membrane of living organisms. They mostly resemble only limited features such as charge distribution, and often fail regarding inhomogeneity between the lipid layers of a bilayer.

2.4 Endosomal sorting complex required for transport

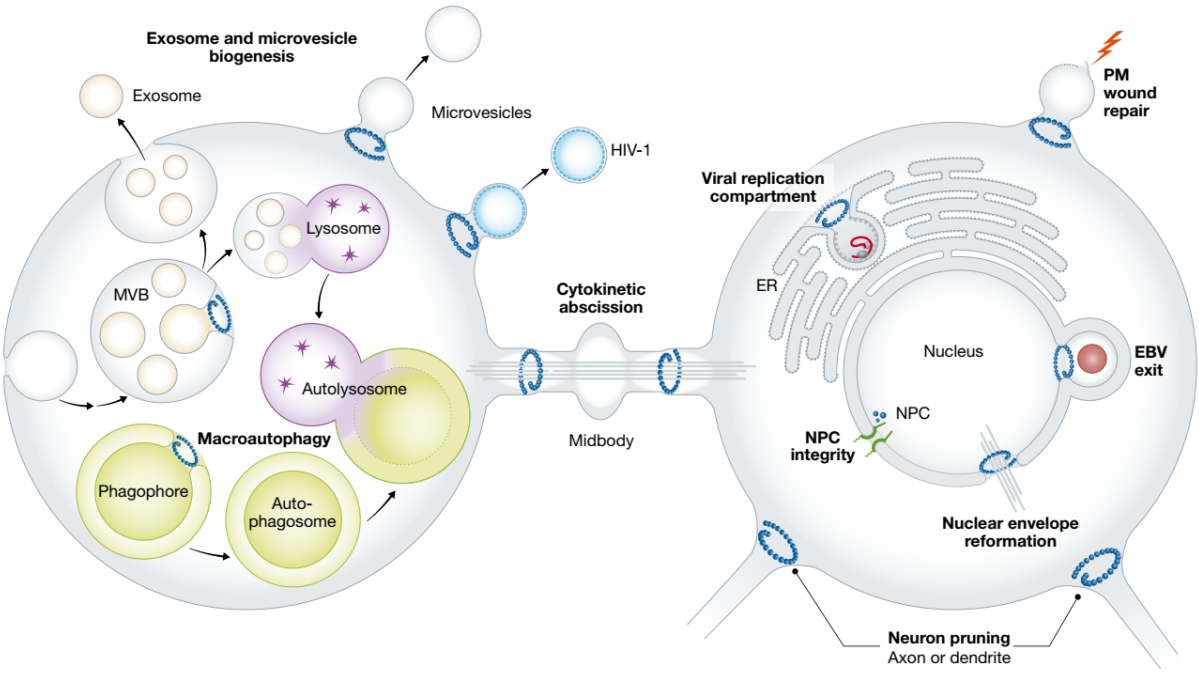

Figure 3 Overview of ESCRT functions in cells. Image taken from Hurley 2015[19].

The endosomal sorting complex required for transport (ESCRT), discovered in the mid 1980ies[20,21] in the biogenesis of multi-vesicular endosomes in budding yeast, and has been investigated ever since. Since then, the involvement of ESCRT or its subcomplexes has been shown in a plethora of functionalities in cells, ranging from neuron pruning[22] to plasma

membrane repair[23] to highjacking by HIV[24] (Fig. 3). The ESCRT machinery is categorized and ordered in four subcomplexes termed ESCRT-0, -I, -II and -III and accessory proteins. Furthermore, ESCRT homologues have been identified in other species beyond yeast ranging from archaea[25] to human[26].

2.4.1 ESCRT-0

The initial complex for the formation of multi-vesicular bodies (MVB) is termed ESCRT-0 and consists of the heterodimer of HSE1 and Vps27, which performs in the cytoplasm[27]. They initialize the MVB pathway by localizing to the endosome via interaction with Phosphatidylinositol 3-phosphate, an important phospholipid for protein trafficking to the membrane, and proteins tagged with ubiquitin moieties[28,29]. They begin the clustering of ubiquitinated targets and start the recruitment of the ESCRT-I complex via Vps27 interaction with Vps23[28].

2.4.2 ESCRT-I

The main role of ESCRT-I is the sorting of cargo into MVBs. It consists of a preformed hetero-tetramer of Vps23, Vps28, Vps37 and MVB12[30]. Subunits of this complex further interact with more ubiquitinated targets and thereby facilitate cargo sorting into MVBs[31]. ESCRT-I subunit Vps28 recruits ESCRT-II to the MVB formation site by interaction with Vps36, thus stabilizing the vesicle neck[32].

2.4.3 ESCRT-II

The heterotetrameric complex of Vps36, Vps22 and two Vps25 proteins build up ESCRT-II[33]. The association of ESCRT-II to the MVB neck is facilitated by binding to Phosphatidylinositol 3-phosphate as well as ubiquitinated targets, which together with the binding of ESCRT-I stabilize the vesicle neck[32]. The subsequent recruitment of ESCRT-III is facilitated by the two Vps25 proteins, which recruit Vps20[34].

2.4.4 ESCRT-III

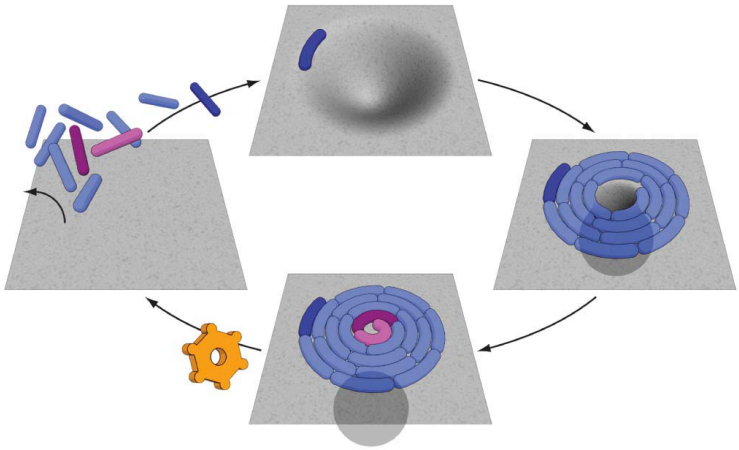

Figure 4 ESCRT-III scission machinery. Clockwise starting from 12 o'clock: Vps20 (dark blue) binds to the membrane, Snf7/Vps32 (light blue) recruits to Vps20 and to form a homomultimeric spiral forcing membrane invagination, Vps24 (purple) and Vps2 (pink) terminate the spiral formation and drive the membrane scission to form an ILV, Vps4 (orange gear) disassembles the spiral from the membrane. Image taken from Wollert et. al 2009[35].

ESCRT-III is the primary scission machinery[36,37] of the MVB pathway and has been shown to facilitate vesicle scission on its own[35]. It consists of Vps20, Snf7 (Vps32), Vps24 and Vps2 and differs from the other subcomplexes in that they do not form multimeric structures in the cytoplasm. ESCRT-III also encompasses the assessor components Did2, Ist1 and Vps60, *vide infra*, next section (2.4.5). Upon recruitment of Vps20 to the membrane, the polymerization of Snf7 on the endosomal membrane is promoted, which starts the assembly of a spiral around the ESCRT-I and -II stabilized neck[32]. The Snf7 spiral formation drives neck constriction and is terminated by Vps24 and Vps2[38] (Fig. 4). The vesicle scission is likely caused by the generated tension within the Snf7 spiral[39], whereas other evidence points to Vps24 and Vps2 to contribute to the scission[23,40].

While spiral formation has been shown *in vitro*, the full mechanism of vesicle scission by the ESCRT-III complex is still being investigated with three hypothesised mechanisms[38].

2.4.5 ESCRT-III associated proteins

There are further additional proteins associated with the disassembly of the ESCRT-III spiral. The disassembly is primarily facilitated by the Vps4[41], a type-1 AAA ATPase. In the cytoplasm Vps4 resides as inactive monomers or dimers[42], which upon recruitment to the membrane by Vps2 assemble into the active complex. The recruitment is further supported by Did2 and Ist1, both have been shown to be involved but not essential for the recruitment of Vps4[43]. The

active Vps4 complex is further stabilized by its cofactor Vta1, which also modulates the ATPase activity[44].

2.5 Cytoskeleton

Cellular shape is dynamically maintained by the cytoskeleton, which is composed of four main filamentous networks that operate on different time and lengths scales. Highly dynamic and rapidly changing structures, like lamellipodia, are maintained by actin microfilaments[45]. Microtubules (MTs) act on longer range and slower time scale compared to actin, and are the main filament to maintain, support and generate the global shape of cells[46,47]. Intermediate filaments differ from the former two by the fact that they are far less dynamic and lack polarity, they provide mechanical support for the plasma membrane[48]. A more recent addition to the group of cytoskeletal proteins are septins which assemble into filaments and rings and function as diffusion barriers and localizations sites for other proteins[49] (Fig.5).

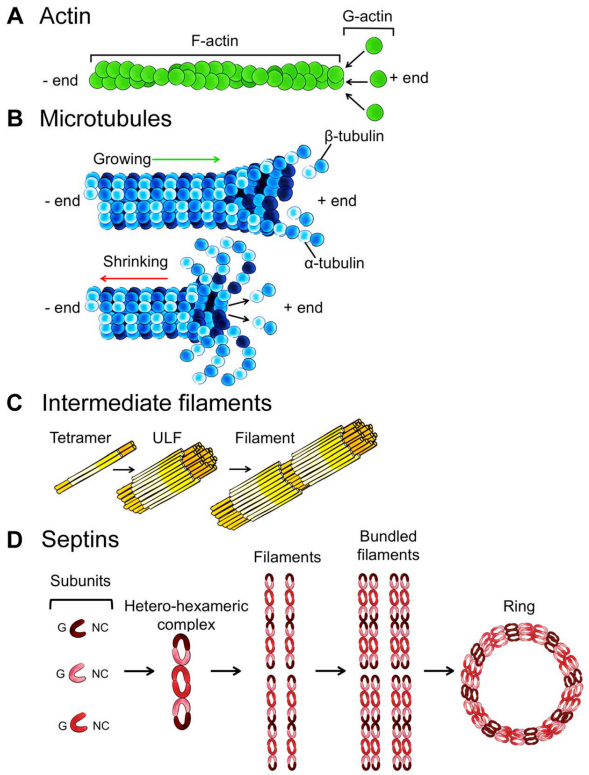

Figure 5 Overview of the four cytoskeletal components. (A) actin filament assembles, (B) (dis)assembly of Microtubules, (C) Assembly of intermediate filaments and (D) Septin assembly into filaments and rings. Image taken from Mostowy 2014[50].

2.5.1 Microtubules

The discovery of MTs in the late 1930ies and their involvement in the mitotic spindle of eukaryotic cells[51] sparked tremendous research efforts into MT-dynamics[52], structure and associated proteins[53] and is still a major subject of research.

Besides being necessary for the maintenance of cellular shape, MTs are also important for the segregation of chromosomes during mitosis[54]. Another important function of MTs is the transport of cargo along them. They serve as rails for motor proteins[55], which transport vesicles and organelles across the cell[55]. Furthermore, in mammalian cells the majority of MTs originate from a MT organizing centre (MTOC) known as the centrosome, but more MTOCs are known in a diverse spectrum of species[56].

MTs are formed from heterodimers of α– and β–tubulin. They form a dynamic filamentous polymer with a 24 nm outer diameter and an intrinsic polarity. MTs exhibit dynamic instability, a permanent switching between polymerisation and depolymerisation[57,58]. This process allows the MTs to explore the cellular space, thereby maintaining the cellular shape and adapting to the cell's environment[59].

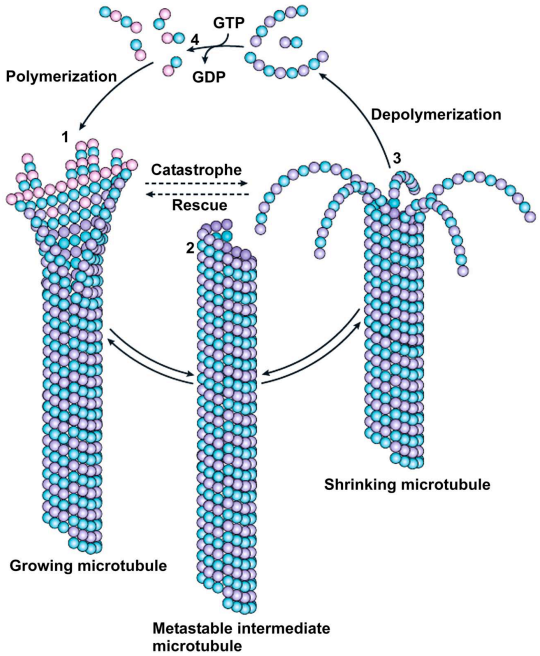

Figure 6 Scheme of the dynamic instability of microtubules. Image taken form Akhmanova and Steinmetz 2008[60].

Energy required for MT-dynamics (Fig. 6) is supplied by the hydrolysis of guanosine-5'-triphosphate (GTP) to guanosine-5'-diphosphate (GDP) by the beta-tubulin subunit. GTP-bound tubulin is incorporated into the MTs during polymerisation. With a delay after incorporation, the GTP is hydrolysed to GDP, which bends the structure of the tubulin dimer

and promoting depolymerisation[61]. Due to the delayed hydrolysis, the MT maintains a GTP cap that is stabilizing the whole MTs, whereas the rest of the MT lattice is GDP bound. This general dynamic behaviour of MTs is further influenced and regulated by other factors, like microtubule associated proteins[46] and other modulators.

2.5.2 Microtubule associated proteins

A large group of proteins known to interact with MTs are called microtubule associated proteins (MAPs). Being initially defined as proteins that co-purify with tubulin[62], this definition has evolved to encompass all proteins specifically binding to tubulin or MTs. Hence, MAPs are crucial for a plethora of cellular functions by affecting MT-dynamics, facilitating transport along MTs and more.

MAPs after the classical definition, like tau or MAP2, are highly abundant in neurons to stabilize MTs in the axon[63]. Other MAPs have been shown to promote assembly like XMAP215[64], induce MT bundling like MAP65[65] and more (for a more detailed overview see Gouveia & Akhmanova 2010[53]). In the following section, the three MAPs used in the experimental part of this work will be discussed in more detail.

2.5.2.1 Stathmin

Stathmin, also known as oncoprotein 18, is an 18 kDa large protein[66] belonging to the group of MT destabilizing regulators. It regulates MTs indirectly by sequestering tubulin[67], thereby reducing the free tubulin concentration and affecting growth velocity and catastrophe frequency[68]. However, direct interaction with MTs has been observed as well, and promotes depolymerization[69].

The sequestration of tubulin by stathmin is regulated in turn by the phosphorylation state of stathmin. If stathmin is dephosphorylated, it binds two tubulin dimers and upon phosphorylation releases at least one dimer[70]. *In vivo*, the phosphorylation is regulated by both signal-transducing kinases as well as cell-regulating kinases on four serine residues[71] (Ser16, 25, 38 and 63).

2.5.2.2 ch-TOG

ch-TOG is a member of the XMAP215/Dis1 family of MT polymerases[72], and the human homologue to XMAP215 from *xenopus*. The basic structure of these proteins are TOG domains, which are known to facilitate the interaction with MT plus ends[73]. ch-TOG contains five TOG domains, similar to XMAP215.

ch-TOG has been shown to act as a MT polymerase, and to increases the growth velocity of the MT[74]. *In vivo*, ch-TOG also interacts with other +TIP tracking proteins such as SLAIN2[75] and TACC3[76] to enhance polymerisation and increase +TIP tracking. It also plays a role as an error correction factor during mitosis by interacting with kinetochores[77].

2.5.2.3 TPX2

TPX2 is known for its involvement during MT-nucleation and is a major target of the Ran pathway[78–80]. Its activity is regulated by importin proteins[74,79]. A clear mechanism of TPX2s function has not been determined yet, but it has been hypothesised that it directly suppresses the off-rate of tubulin from the +TIP of the MT during polymerisation as well as depolymerisation[81].

In vivo, TPX2 is important for the establishment of a stable bipolar spindle during chromatin-dependent spindle assembly[81]. Furthermore, TPX2 has been shown to be involved in RanGTP-dependent and independent MT branching[81]. It also recruits the plus-end directed motor Xlp2, which TPX2 recruits when bound to MTs[78,82], and regulates Aurora A kinase activity by promoting its autophosphorylation at the mitotic spindle[83]. *In vitro*, TPX2 addition has shown that, in low concentrations, it increases the lifetime of MTs[74], whereas high concentrations promote tubulin aggregation and the emergence of interconnected MT bundles[84].

2.6 Cytoskeleton reorganization by signalling networks

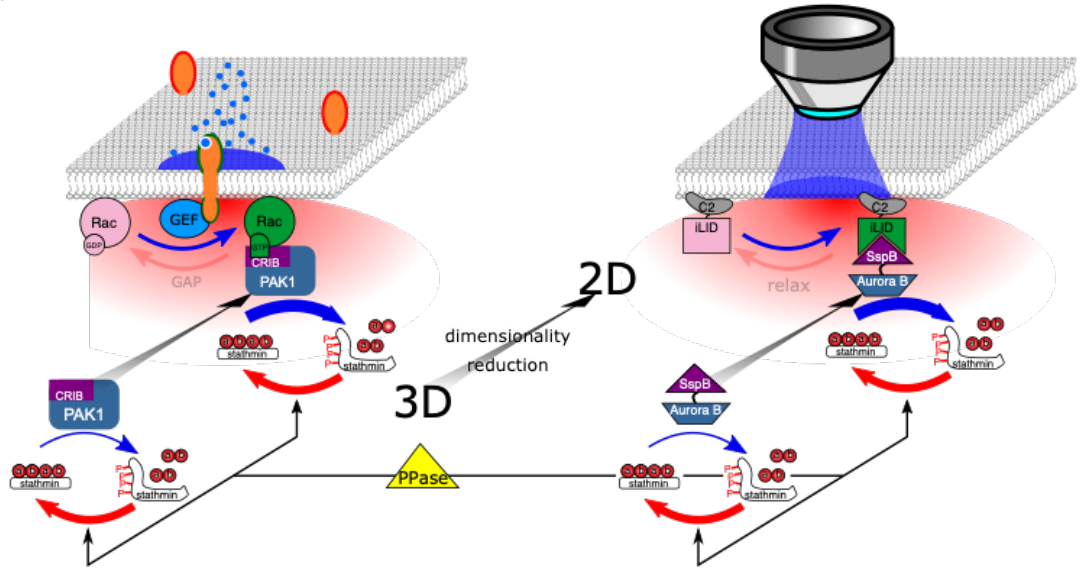

Figure 7 Biomimetic principles of synMMS. Scheme of the natural (left) and the biomimetic (right) signal transduction to the MT-cytoskeleton. Lower cycles: before a stimulus is given and, in the lumen, distant from the membrane the (de)phosphorylation cycle of stathmin is dominated by the higher PPase activity (red arrow) in comparison to the kinase (natural PAK1, synthetic AuroraB, blue arrow), which maintains a low steady state phosphorylation level of stathmin (P-) supressing tubulin polymerisation by sequestration of free tubulin. Upper cycle: Upon and during stimulation the cell (left) reacts to a extracellular morphogen (blue dots) by receptor activation (orange). The locally activated receptor on the membrane recruits the GEF to the membrane and activates the GTPase Rac by nucleotide exchange (pink-to-green). The activated Rac recruits PAK1 via its CRIB domain to the membrane thereby reducing the dimensionality of PAK1 and increases its concentration on the membrane drastically. This shifts the balance of the (de)phosphorylation cycle proximal to the membrane in favour of the kinase. This locally increases the phosphorylation level of stathmin which in turn releases the previously sequestered tubulin. In the biomimetic system, the morphogen signal is replaced by a light stimulus, which activates the photo dimerizer system iLID/SspB. This locally enhances the concentration of the kinase Aurora which acts similar on stathmin to PAK1. Image modified from Gavriljuk et. al 2021[70].

Cells constantly perceive a plethora of signals from their environment and have to adjust their identity accordingly to these signals. These external signals are processed by various protein networks within the cell, which then trigger changes in the cells such as cell motility, proliferation, and more.

Changes in the MT-cytoskeleton, and by extension changes in cells morphology, are caused by the activation of different MAPs through these signalling networks. One of these signalling networks is the canonical Rac1-PAK1-stathmin MT-regulatory network[85–87]. The morphogen signal causes the activation of Rac1 which leads to the recruitment and subsequent activation and localization of PAK1 on the plasma membrane. PAK1 then phosphorylates stathmin and thereby weaking its ability to sequester tubulin which in turn increases the fraction of free tubulin dimers for MT-polymerisation (Fig. 7, left).

The recruitment of these effectors to the membrane, upon active signalling additionally reduces the dimensionality[88,89] from three dimensions in the cytosol to two dimensions on the

membrane. This substantially increases the concentration on the membrane compared to that in the cytosol and, leading to higher protein activity on the membrane. Therefore, it does not surprise that geometrical features of the membrane affect signalling[90].

2.6.1 A biomimetic signalling system

Inspired by this MT-regulatory network, we designed a biomimetic signalling system with homologous properties (Fig. 7, right). In our system, the morphogen signal is mimicked by blue light which activates the optical dimerizer system of the improved Light-inducible Dimer/Stringent starvation protein B (iLID/SspB)[91]. The iLID component of the dimerizer system was designed to be localized to the membrane of liposomes whereas the SspB was fused to the stathmin phosphorylating kinase AuroraB[92]. This system is able to capture the dimensionality reduction principle of the MT-regulatory network. The kinase AuroraB affects the phosphorylation state of the the MT regulator stathmin (2.5.3.1) and influences its effects on MT-dynamics. The dephosphorylation of stathmin, in our system, is controlled by the protein phosphatase lambda (PPλ). The kinase and phosphatase together form a (de)phosphorylation cycle for stathmin. The balance of this (de)phosphorylation cycle can be locally influenced by the photo activation of the system, which shifts the balance of the cycle form the dephosphorylated state of stathmin in the lumen/bulk to the phosphorylated state close to the membrane activated.

3. Objective

The human drive to fully understand living organisms as well as generating them *de novo* led to the emergence of the interdisciplinary field of synthetic biology, combining approaches and rationales from engineering, molecular biology, systems biology and more. But life as we know it today evolved over billions of years and developed to tremendous degrees of complexity. One major development during the evolution of cells was the feature to be separated from the environment and thereby develop an internal state which differs from the state of the environment, but which can still be affected by it.

To mimic these features, encapsulation methods were developed to generate liposomes that could be filled with any complex mixture of macromolecules. Most of these methods are limited in their applicability with proteins due to the involvement of oil phases that harm proteins, especially membrane associated ones, but are necessary for lipid solubility. But cells on their own evolved mechanisms to incorporate and separate matter from either their environment or within themselves.

The objective for this work is to develop and establish an encapsulation method heavily inspired by the natural process of non-selective autophagy to encapsulate a synthetic cytoplasm into ILV within a GUV. Together with the recent developments and insights into the scission mechanism of ESCRT, specifically the subcomplex ESCRT-III, and its capability to encapsulate fluorescenct proteins like GFP into ILV[35], this machinery showed promising features to achieve effective encapsulation of proteins beyond GFP.

To this end the ESCRT-III scission machinery from *entamoeba histolytic*a was chosen to establish it as a protein-based method for encapsulation. To further investigate the capability of the encapsulation machinery to encapsulate any given synthetic cytoplasm, the subsystems of the synMMS[70] were encapsulated, developed in the lab. Finally, the complete encapsulation of synMMS was investigated to illuminate features beyond previously published results.

4. Materials & Methods

4.1 Materials

4.1.1 Commercial proteins and chemicals

Table 1 Chemicals and commercial proteins

Protein / chemical	**Manufacturer / Supplier**
1,4 Dithiothreitol (DTT)	Biomol (Hamburg)
Adenosine 5' triphosphate disodium salt (ATP)	Sigma-Aldrich (München)
Guanosine 5'-triphosphate sodium salt hydrate (GTP)	Sigma-Aldrich (München)
Mineral oil	Sigma-Aldrich (München)
Nochromix, glass cleaning agent	Sigma-Aldrich (München)
PIPES	Sigma-Aldrich (München)
Avidin *BioChemica*	PanReac AppliChem (Darmstadt)
Dimethyloctadecyl[3-(trimethoxysilyl)propyl]ammonium chloride solution	Sigma-Aldrich (München)
Albumin, Biotin labelled bovine	Sigma-Aldrich (München)
DNase I from bovine pancreas	Sigma-Aldrich (München)
cOmplete Tablets EDTA-free	Roche (Basel, Schweiz)
Geranylgeranylpyrophosphat (GGPP)	Sigma-Aldrich (München)
3-[(3-Cholamidopropyl)dimethylammonio]-1-propanesulfonate hydrate (CHAPS)	Sigma-Aldrich (München)
Riboflavin-5'-monophosphat natrium salt hydrate	Sigma-Aldrich (München)
Guanosine-5'-[(α,β)-methyleno]triphosphate, sodium salt (GMPCPP)	Jena Bioscience (Jena)
SNAP-Surface 594	New England BioLabs (Frankfurt am Main)
AccuPrime™ Taq Polymerase	Thermo Fisher Scientific (München)
FastDigest restriction enzymes	Thermo Fisher Scientific (München)
T4 DNA Polymerase	New England BioLabs (Frankfurt am Main)
FuGENE® HD Transfection Reagent	Promega (Madison, USA)
NHS-Alexa488	Thermo Fisher Scientific (München)
NHS-Alexa647	Thermo Fisher Scientific (München)
NHS-Atto532	Atto-Tec (Siegen)
NHS-Atto542	Atto-Tec (Siegen)
NHS-Atto655	Atto-Tec (Siegen)

4.1.2 Cell strains

Escherichia coli strains

XL10 Gold	Stratagene (San Diego, USA)
BL21 (DE3) RIL	Thermo Fisher Scientific (München)

Insect cell strains

Sf9	Andrea Musacchio, MPI Dortmund
TnaO38	Andrea Musacchio, MPI Dortmund

4.1.3 Culture media

Table 2 Culture media

SOC:	20 g/L BactoTrypton 5 g/L yeast extract 0.58 g/L NaCl 0.19 g KCl 2.03 g/L $MgCl_2$x 6 H_2O 2.46 g/L $MgSO_4$ x 7 H_2O 2 % Glucose
SOB:	20 g/L BactoTrypton 5 g/L yeast extract 0.58 g/L NaCl 0.19 g/L KCl 2.03 g/L $MgCl_2$x 6 H_2O 2.46 g/L $MgSO_4$ x 7 H_2O
LB:	10 g/L BactoTrypton 5 g/L yeast extract 10 g/L NaCl pH 7.4
TB:	12 g/L BactoTrypton 24 g/L yeast extract 4 ml/L glycerin 2,31 g/L KH_2PO_4 12,54 g/L K_2HPO_4
SF-900™ II SFM	ThermoFisher Scientific

4.1.4 Vectors

Table 3 Vector plasmids for protein expression

Vector backbone	**Protein**	**Creator**
pET28a (Kan)	GGTase I β	Konstantin Gavriljuk, MPI Do
pGATEV (Amp)	RabGGTase β	Konstantin Gavriljuk, MPI Do
pRK793 (Amp)	TEV	Konstantin Gavriljuk, MPI Do
	Sortase A	Peter Bieling, MPI Do
pET24-H10T (Kan)	Strep-EGFP	Konstantin Gavriljuk, MPI Do
pMAL (Amp)	ehVPS20	This work
pMAL (Amp)	ehVPS20ΔC (1-173)	This work
pMAL (Amp)	ehVPS32	This work
pMAL (Amp)	ehVPS24	This work
pMAL (Amp)	ehVPS2	This work
pGEX2rbs (Amp)	Gly-SspB-AuroraB (55-344) / INCENP (835-903) bicistronic vector	Konstantin Gavriljuk, MPI Do
pET24-H10T (Kan)	Gly-CRIB-PPλ	Konstantin Gavriljuk, MPI Do
pET24-H10T (Kan)	Gly-Stathmin-Cys	Konstantin Gavriljuk, MPI Do
pET24-H10T (Kan)	Gly-C2lact-iLID	Konstantin Gavriljuk, MPI Do
pET24-H10T (Kan)	Gly-iLID-tRac1	Konstantin Gavriljuk, MPI Do
pFastBac-2xStrepHis (Amp)	Gly-2xCRIB-chTOG	Konstantin Gavriljuk, MPI Do
pFastBac-2xStrepHis (Amp)	Gly-TPX2	Konstantin Gavriljuk, MPI Do

4.1.5 Primers and Genes constructs

Primers were supplied by Eurofins Genomics (Ebersberg)

Sequencing primers

T7 Promoter	TAATACGACTCACTATAGGG
T7 Terminator	GCTAGTTATTGCTCAGCGG
5’ pMAL	GTGATCAACGCCGCCAGC
3’ pMAL	GCCCCAAGGGGTTATGCTAG
5’ pTac	CCGACATCATAACGGTTCTGGC
3’ pTac	GATTTTCCCTTAAGGAGTACCTAC
5’ polyhedrin fwd	AAATGATAACCATCTCGC
3’ FastBac	GGGAGGTGTGGGAGGTTT

For longer DNA fragments that couldn’t be sequenced with these standard primers, specific primers were designed ca. 50 bp preceding the position where sequencing with standard primers stopped.

Amplification primers

5’ pET24	AGAACCTGTACTTTCAGGGC
3’ pET24	TTAGCAGCCGGATCTCAGGC
5’ pMAL	TCTTTATTTTCAGGGCCAT
3’ pMAL	GCATCTAGAGGGCCCGGATCCTTA

Gene constructs

Gene constructs were ordered and synthesized by Eurofins Genomics (Ebersberg). All genes were designed for immediate sequence and ligation independent cloning into the target vectors.

4.1.6 Laboratory equipment

Leica TCS SP8	Leica Microsystem (Wetzlar)
Emulsiflex C5	Avestin (Mannheim)
Microfluidizer LM10	Microfluidics (Westwood, USA)
FPLC Äkta Purifier 10	Cytiva (former GE Healthcare Life Science; Freiburg)
FPLC Äkta Pure 25L	Cytiva (Freiburg)
DU 800 Spectrophotometer	Beckman Coulter (Krefeld)
Spectrophotometer	Shimadzu (Duisburg)
Tabletop Ultracentrifuge	Beckman Coulter (Krefeld)

Not specified equipment is considered laboratory standard.

4.1.7 Software and tools

Microsoft Office	Microsoft (Redmond, USA)
Inkscape	Inkscape
OriginPro 9.0G	OriginLab (Northampton, USA)
DNASTAR Lasergene	DNASTAR Inc. (Madison, USA)
ImageJ	National Institutes of Health (Bethesda, USA)
Matlab 2019b	MathWorks Inc. (Natick, USA)

4.1.8 Chromatography columns and resins

GSTrap™ FF	Cytiva (former GE Healthcare Life Science; Freiburg)
GSTrap™ HP	Cytiva (former GE Healthcare Life Science; Freiburg)
MBPTrap™ HP	Cytiva (former GE Healthcare Life Science; Freiburg)
XK 16/600 Superdex 75 p.g.	Cytiva (former GE Healthcare Life Science; Freiburg)
XK 16/600 Superdex 200 p.g.	Cytiva (former GE Healthcare Life Science; Freiburg)
XK 26/600 Superdex 75 p.g.	Cytiva (former GE Healthcare Life Science; Freiburg)
XK 26/600 Superdex 200 p.g.	Cytiva (former GE Healthcare Life Science; Freiburg)
XK 10/300 Superdex 75 p.g.	Cytiva (former GE Healthcare Life Science; Freiburg)
Superose 6 Increase 10/300	Cytiva (former GE Healthcare Life Science; Freiburg)
HiPrep™ 26/60 Desalting	Cytiva (former GE Healthcare Life Science; Freiburg)
Ni-NTA Superflow	Qiagen (Hilden)

4.1.9 Special materials

Illustra™ NAP™-5 Columns	GE Healthcare Life Science (Freiburg)
Pierce® Detergent Removal Spin Columns 0.5 mL	Thermo Fisher Scientific (München)
NucleoSpin® Plasmid Kit	Macherey-Nagel (Düren)
NucleoBond® Xtra Midi Plus EF Kit	Macherey-Nagel (Düren)
NucleoSpin® Gel and PCR Clean-up Kit	Macherey-Nagel (Düren)
Amicon Ultra 0.5/4/15 mL 10/30/50/100K Concentrator	Merck-Millipore (Schwalbach)
Amicon Stirred Cell with 10K ultrafiltration membrane	Merck-Millipore (Schwalbach)
Dialysis tubing SnakeSkin 10K	Thermo Fisher Scientific (München)
Glass Capillaries GC129T-10	Harvard Apparatus Limited (Holliston, USA)

4.2 Biomolecular methods

4.2.1 Polymerase chain reaction

For PCRs AccuPrime™ Taq Polymerase (Thermo Fisher Scientific) was used as stated by manufacture protocol. Usually 100 ng of DNA-fragments were used per reaction.

Melting temperature for primers was calculated with this formula

$$Meltingtemperature = 69.3 + 0.41 \times GC - \frac{650}{N}$$

and designed to yield melting temperatures of 58-62 °C. With GC being the content of guanine and cytosine in % and N being the length of the primer sequence.

The PCR program used was as followed:

1. 95 °C 3 min
2. 95 °C 1 min
3. 58 to 62 °C 45 s
4. 72 °C 90 s, 30x looping back to 2.
5. 72 °C 10 min

The finished reaction was further processed as described in the following section (4.2.2).

4.2.2 Sequence and ligation independent cloning

For this cloning method, the vectors were digested as in section 4.2.3. Linear DNA-fragments were designed with 20 base pair homology overhangs to the target vector on both ends. For the reaction 150 ng of vector and 300 ng of insert were mixed with 1x NEB 2.1-buffer and 0.5 U T4-polymerase in 20 µL reaction volume. The reaction was incubated for 30 minutes at 22 °C to generate 3' overhangs on vector and insert. The reaction was stopped by adding 1 mM of any dNTP. 5 µL of T4 ligation buffer was added to the reaction and incubated for further 30 minutes at 37 °C to anneal the fragments. The finished reaction was either used immediately for transformation (4.2.4) or stored at –20 °C.

4.2.3 Restriction digest

Vectors used for Sequence and ligation independent cloning were digested with FastDigest™ enzymes (Thermo Fisher Scientific).

pET24-H10T digested with EheI
pMAL digested with NdeI and BamHI
pFastBac-2xStrepHis digested with EheI and HindIII

4.2.4 Heat-shock transformation

For the transformation into different *E. coli* strains 100 µL of competent cells (4.2.5) were mixed with 3.5 µL of 2.25 M DTT, 1 µL plasmid-DNA or 5 µL SLIC reaction and incubated for 30 minutes on ice followed by a 45 second heat-shock at 42 °C and additional 2 minutes on ice. After this 900 µL SOC was added to the reaction and incubated at 37 °C and 200 rpm for 1 hour. 100 µL of the solution was dispersed a LB-agar plate with the respective antibiotics. For transformations in expression strains, the regenerated cells were spun down and the full cell pellet was dispersed onto the plate. Plates were incubated at 37 °C overnight.

4.2.5 Preparation of competent cells

To generate competent cells, were picked from an agar plate and grown over night in 5 mL SOB at 30 °C. The next day 250 mL of SOB were inoculated with 50-200 µL of the overnight culture and grown to a OD600 of 0.6 at 20 °C and 130 rpm. The culture was harvested at 1800 g and 4 °C for 10 minutes. The cell pellet was resuspended in 80 mL of 4 °C and CCMB80 buffer (Teknova) and incubated for further 20 minutes on ice. The cells were pelleted as before and then resuspended in 10 mL 4 °C CCMB80 buffer. The competent cells were aliquoted, frozen in liquid nitrogen and stored at -80 °C.

4.2.6 DNA vector isolation

Plasmid vectors were purified with the NucleoSpin® Plasmid Kit (Macherey-Nagel) following manufacturer's protocols. Vectors used for sequence and ligation independent cloning (4.2.2) were purified with NucleoBond® Xtra Midi Plus EF Kit (Macherey-Nagel) following manufacturer's protocols. Plasmid concentration was determined with a NanoDrop-spectrophotometer.

4.2.7 Gel-electrophoresis

DNA-fragments from PCR or restriction digests were purified with a 1 % agarose-gel stained with RedSafe™ NucleicAcidStaining Solution, running at 50 mA in TAE-buffer. DNA was mixed with loading buffer prior to loading on the gel.

TAE-buffer: 40 mM Tris pH 8, 20 mM Acidic acid, 1 mM EDTA
5x Loading-buffer: 25 mM Tris pH 7.6, 0.5 % Orange G, 0.5 mM EDTA, 30 % (v/v) Glycerol
The DNA-band in the gel was purified using the NucleoSpin® Gel and PCR Clean-up Kit (Macherey-Nagel) following producer protocols. Plasmid concentration was determined with a NanoDrop-spectrometer.

4.2.8 DNA sequencing

Sequencing reactions were prepared following protocol of the LightTube Barcode sequencing (Eurofins genomics, Ebersberg) and sent for sequencing. Sequencing data were evaluated with the program suite DNASTAR Lasergene (DNASTAR).

4.2.9 Bacterial cryo-stocks

For long term storage cryo-cultures of transfected cells were prepared. For this a 1:1 mix of a liquid *E. coli* cell culture and Cryo-buffer was prepared and frozen in liquid nitrogen and stored at -80 °C.

Cryo-buffer: 25 mM Tris pH 8, 100 mM $MgSO_4$, 65 % (v/v) Glycerol

4.2.10 Protein expression in *Escherichia coli*

Cells for protein purification (4.3.1) were grown specifically by target protein as in Tab. 5. For this 20 mL LB precultures with respective antibiotics (Tab. 4) were prepared and grown at 30 °C at 200 rpm overnight.

Table 4 Antibiotic conditions for Escherichia coli

Antibiotic	**Concentration in media**
Carbenicillin/Ampicillin	100 mg/L
Chloramphenicol	34 mg/L
Kanamycin	50 mg/L

The next morning, the preculture was spun down at 3000 g for one minute and supernatant was discarded. The cell pellets were resuspended in 10 mL TB and added to the 12 L TB main culture. The main culture was grown to an OD600 of 0.5 (for 18 °C expression) or 1 (for 37 °C expression). Protein expression was induced by adding IPTG to a final concentration of 0.2 mM (for 18 °C expression) or 0.5 mM (for 37 °C expression) with expression times varying, by target protein (Tab. 5). After the expression time cells were harvested by centrifuging for 10 minutes at 5000 xg. The cell pellets were suspended in lysis buffer (4.3.6) and stored frozen at -20 °C until further purified (4.3).

Table 5 Protein expression conditions

Protein	Temperature	Expression Time
ehVps2	37 °C	6 h
ehVps20dC	37 °C	6 h
ehVps24	37 °C	6 h
ehVps32	37 °C	6 h
Gly-SspB-AuroraB/INCENP	18 °C	18 h
Gly-iLID-tRac1	18 °C	18 h
Gly-C2lact-iLID	18 °C	18 h
Gly-CRIB-PPl	18 °C	18 h
Gly-Stathmin-Cys	18 °C	18 h

4.2.11 Protein expression in Insect cells

For protein expression in insect cells, 2-4 µg of the plasmid DNA were mixed with 250 µl of SF-900^{TM} media (Thermo Fisher Scientific) and incubated with 4 µl FUGENE transfection reagent (Promega) for 20 min at room temperature. 3 ml of 3x10^5 SF9 cells were transferred into a sterile culture dish. After the cells had time to adhere for 30 min at 27 °C, the transfection mix was carefully added to the cells and incubated for 5 days at 27 °C.

Next, the transfected cells were resuspended with 10 ml of 1x10^6 SF9 cells. Following 4 days of incubation, the transfected cells were centrifuged for 10 min at 150 xg and the virus containing supernatant was filtered through a 0.2 µm syringe filter. To further amplify the virus, 50 ml of 1x10^6 SF9 cells were transfected with 500 µl of virus and were again incubated for 4 days shaking at 200 rpm at 27 °C. Following the virus amplification, the virus was separated through centrifugation and filtration.

To start protein expression, 2 L of 1x10^6 TnaO38 cells were infected by addition of the virus with a 1 to 50 ratio and the proteins were expressed over 3 days. After protein expression, the cells were harvested at 2000 g for 20 min at 18 °C and the cell pellets was resuspended in lysis buffer (4.3.6) and frozen in liquid nitrogen and stored at -80 °C until further purification (4.3).

4.3 Biochemical methods

4.3.1 Cell lysis

E. coli cell pellets (4.2.10) were thawed at 4 °C and 50 mg DNase I (Sigma-Aldrich), 50 mg ATP (Sigma-Aldrich) and one cOmplete™ pill (Roche) was added to 100 mL Pellet each. The pellet was homogenized prior to lysis by three runs through an Emulsiflex C5 or a MicroFluidizer pre-equilibrated in lysis buffer (See list of buffers, 4.3.6).

Insect Cell pellets (4.3.11) were thawed at 4 °C and 50 mg DNAse I (Sigma-Aldrich), 50 mg ATP (Sigma-Aldrich) and one cOmplete™ pill (Roche) was added to 100 mL Pellet each. The pellets were lysed with 10 strokes in a dounce homogenizer.

The lysate was centrifuged for 45 minutes at 20000 xg. The supernatant was decanted and filtered through a 0.8 µm syringe filter before further purification via affinity chromatography (4.3.2, 4.3.3, 4.3.4).

4.3.2 Glutathione *S*-transferase affinity chromatography

After lysis (4.3.1), GST-tagged Gly-SspB-AuroraB/INCENP was run over two self-packed GSH HP columns (ca. 25 ml column volume (cv)) with 1 mL/min. After initial binding, the columns were washed with one cv of lysis buffer (4.3.6) with additional 10 mM ATP and further washed with one cv lysis buffer or till a baseline was reached. The protein was eluted with lysis buffer plus 20 mM L-Glutathione and the eluate was pooled. The L-Glutathione was removed by running it over a desalting column into lysis buffer. The GST-tag of the desalted fractions was cut off by digestion with 50 µM TEV overnight at 4 °C under slow agitation. The uncut protein and the separated GST-tag were separated by another run over the GSH HP columns. The cleaved protein was pooled and further purified via size exclusion chromatography (4.3.5).

4.3.3 Maltose binding protein affinity chromatography

Supernatant (4.3.1) of proteins tagged with maltose binding protein (MBP; all ESCRT-III proteins) were cycled over a 5 mL MBPtrap column at 4 °C for 2-3 hours at 2 mL/min. The protein saturated column was washed with lysis buffer for 5 cv or until a baseline was reached. The MBP-tagged protein was eluted with lysis buffer containing 10 mM maltose.

For removal of maltose after elution, the proteins were desalted by size exclusion chromatography on a XK 26/60 Superdex 200 p.g. The MBP-tag was cut off by digestion with 50 µM TEV overnight at 4 °C under slow agitation. The MBP-tag and the target protein were separated after digestion by another run over the MBPtrap column and the cleaved protein was pooled afterwards for further purification via size exclusion chromatography (4.3.5).

4.3.4 Polyhistidine-tag affinity chromatography

For purification of His-tagged proteins, a self-packed Ni-NTA superflow column with 25 mL cv was used. The supernatant (4.3.1) was cycled over the equilibrated column, pre-equilibrated in lysis buffer, for 2-3 hours at 3 mL/min. After cycling, the column was washed in two steps for one cv with buffer containing 40 mM and 60 mM Imidazole. The target protein was eluted with buffer containing 500 mM imidazole at 1 mL/min. The eluted protein was pooled and the Imidazole was removed by running it over a desalting column into lysis buffer. TEV digestion with 50 µM TEV was performed during dialysis. The His-tag was removed with another run over the Ni-NTA column in lysis buffer (4.3.6) containing 20 mM Imidazole. The protein was pooled for further purification (4.3.5).

4.3.5 Size exclusion chromatography

To enhance protein purity beyond affinity chromatography, size exclusion chromatography (SEC) was performed. For this, prepacked Superdex or Superose columns (4.1.8) were chosen according to protein size and protein amount after affinity chromatography. The SEC column was equilibrated with SEC buffer (varying by protein, 4.3.6) prior to usage.

Proteins were concentrated with Amicon Ultra Concentrators prior to sample injection via a 0.5 – 5 mL sample loop. The concentrated sample was spun for 10 minutes at 13000 xg to remove aggregates formed during concentration before SEC. Proteins that formed aggregates

during spin concentration (Gly-SspB-AuroraB, all ESCRT-III proteins used) weren't concentrated, but rather injected using a 15 mL sample loop.

After the column specific void volume, 0.5 – 3 mL fractions were collected. Protein content of the fractions was verified by SDS-PAGE (4.4.1) and fractions containing the purified target protein were pooled. If necessary, multiple SECs were performed and pooled per purification dependent on total protein amount considering the protein loading limit of the SEC column. The pooled fractions were concentrated to the desired volume via Amicon Ultra Concentrators or, for proteins that aggregated during spin concentration (Gly-SspB-AuroraB, all ESCRT-III proteins used), with a Amicon Stirred Cell.

Protein concentration was measured by Bradford assay (4.4.2, all but ESCRT-III proteins) or BCA assay (4.4.3, all ESCRT-III proteins). The protein was aliquoted, frozen, and stored at -80 °C until further use or directly functionalized (4.3.7) and/or labelled (4.3.8, 4.3.9, 4.3.10).

4.3.6 Purification buffers

Table 6 Purification buffers

Buffer name	**Buffer composition**
Lysis buffer for ESCRT-III proteins	20 mM Hepes pH 7.2 500 mM NaCl 2 mM $MgCl_2$ 2 mM DTT
Lysis buffer for AuroraB	50 mM Hepes pH 7.3 500 mM NaCl 2 mM $MgCl_2$ 5 mM DTT 5 % Glycerol
Lysis buffer for all other proteins	50 mM Hepes pH 7.2 500 mM NaCl 2 mM $MgCl_2$ 5 mM DTT
SEC buffer for ESCRT-III proteins	20 mM Hepes pH 7.2 200 mM NaCl 2 mM $MgCl_2$ 2 mM TCEP
SEC buffer for AuroraB	50 mM Hepes pH 7.3 200 mM NaCl 2 mM $MgCl_2$ 5 mM DTT
SEC buffer for all other proteins	50 mM Hepes pH 7.3 200 mM NaCl 2 mM $MgCl_2$ 2 mM TCEP

4.3.7 Enzymatic prenylation with detergent

To localize Gly-iLID-tRac1 to the membrane, the protein had to be linked covalently to a geranylgeranyl lipid anchor. For this, purified GGTase I β was used. The reaction was performed in glass vials. The detergent CHAPS was used to preserve the solubility of the prenylated protein for the course of the purification.

The enzymatic reaction was composed as follows with a total volume of 3 mL:

ca. 460 nmol GGPP (One Vial)
3 mg Gly-iLID-tRac1
1:10 GGTase I (with respect to Rac1)
50 mM Hepes, pH 7.5
50 mM NaCl
2 mM $MgCl_2$
10 % Glycerol
10 µM $ZnSO_4$
2 % CHAPS
2 mM DTT

The reaction was incubated at 4 °C under constant rotation overnight. After incubation, the sample was spun for 10 minutes at 14000 xg to remove formed aggregates prior to SEC. For SEC, a XK 16/600 Superdex 75 p.g. was equilibrated with prenylation buffer (50 mM Hepes, pH 7.5, 50 mM NaCl, 2 mM $MgCl_2$, 0.5 % CHAPS, 2 mM DTT). The fractions containing the prenylated protein were pooled and concentrated to 250 µL in a Amicon Ultra Concentrator saturated with 0.5 mg BSA. The concentration of the concentrated protein was measured with using absorption at 280 nm and RabGGTase β was added in a 1:1 molar ratio to the sample, to preserve protein solubility after detergent removal.

To remove the detergent, a buffer exchange of the sample was performed over a NAP™-5 column. For this, the NAP™-5 column was equilibrated with prenylation buffer without CHAPS and saturated with 1 mg BSA before the buffer exchange. The buffer exchanged sample was concentrated to 100 µL in an Amicon Ultra Concentrator saturated with 0.2 mg BSA. To finalize the prenylation, left over detergent was removed with a Pierce® detergent removal column following manufacturer's protocol, but additionally saturated with 0.1 mg BSA. The protein concentration was determined by Bradford assay (4.4.2) and the protein was aliquoted, frozen, and stored at -80 °C or immediately labelled (4.3.8, 4.3.9, 4.3.10).

4.3.8 Tubulin purification from pig brain

Tubulin was purified from pig brains following the standard method developed by Castoldi and Popov (2003)[93].

Fresh pig brains, preferably slaughtered less than 6 h before purification, with removed meninges and brain stem were lysed in depolymerization Buffer (50 mM MES pH 6.6, 1 mM $CaCl_2$) using a ratio of 1.5 buffer/brain (L/kg) and 1 mL of 1 M PMSF, by blending for 1 minute at low speed and 2 times 1 minute at high speed with 2-minute breaks on ice in between to prevent overheating. The lysate was centrifuged for 60 min at 4 °C at 28000 xg.

The supernatant was collected and supplemented with polymerization buffer (555 mM PIPES pH 6.9, 5.5 mM $MgCl_2$, 11.1 mM EGTA, 55 % glycerol), ATP and GTP to the final concentration of 333 mM PIPES, 1.5 mM ATP, and 0.5 mM GTP. This mixture was incubated for 60 min at 37 °C to polymerize the tubulin. The polymerized solution was centrifuged for 30 min at 37 °C at 200000 xg.

The supernatant was removed and pooled (to increase tubulin yield, the supernatant can be polymerized a second time) while the pellets were resuspended in cold depolymerization buffer on ice. The depolymerized solution was centrifuged for 20 min at 4 °C at 140000 xg.

The supernatant was pooled and supplemented with polymerization buffer and incubated again as above. This time the pellet was resuspended in cold BRB80 buffer (80 mM PIPES pH 6.8, 1 mM $MgCl_2$, 0.2 mM EGTA). The sample was centrifuged for 20 minutes at 4 °C at 140000 xg and the tubulin containing supernatant was pooled.

Tubulin concentration was determined by Bradford assay (4.4.2) and adjusted to 200 µM with BRB80, frozen, and stored at −150 °C until further use.

4.3.9 Fluorescence-dye labelling of tubulin

Tubulin was labelled with NHS-Alexa647 or -Alexa488 (Thermo Fisher Scientific) according to a modified method based on the method developed by Hyman (1991)[94]. 50 mg of purified tubulin were polymerized with 2.5 mM $MgCl_2$, 1 mM GTP and 33 (v/v) % glycerol for 30 minutes at 37 °C. The polymerized tubulin was loaded onto a 37 °C warm high pH cushion (100 mM Hepes pH 8.6, 1 mM $MgCl_2$, 1 mM EGTA, 0.5 mM GTP, 60 (v/v) % glycerol) and spun at 400000 xg for 45 minutes at 37 °C. The supernatant was removed, and the interface of the cushion was rinsed twice with 37 °C labelling buffer (100 mM Hepes pH 8.6, 1 mM $MgCl_2$, 1 mM EGTA, 0.5 mM GTP, 64 (v/v) % glycerol). The cushion was removed afterwards, and the pellet was resuspended in 4 °C labelling buffer until completely dissolved.

The NHS-dye was dissolved in DMSO and a 7.5-fold molar excess was added to the solubilized MTs. The labelling reaction was kept at 37 °C for 30 minutes and gently mixed every 5 minutes. After the incubation was finished, the reaction was added on top of a 37 °C warm low pH cushion (80 mM PIPES pH 6.8, 1 mM $MgCl_2$, 0.2 mM EGTA, 60 (v/v) % glycerol) and spun at 400000 xg for 25 minutes at 37 °C. After the spin, the supernatant was removed and the cushion rinsed twice with 37 °C warm BRB80 buffer. The cushion was removed, and the pellet was resuspended in 0.6 mL ice cold depolymeristation buffer (100 mM K-glutamate pH 7, 1 mM GTP, 1 mM $MgCl_2$). The resuspended pellet was incubated on ice for 20 minutes and then spun at 125000 xg at 4 °C for 10 minutes. The supernatant was decanted and supplemented with 2.5 mM $MgCl_2$, 1 mM GTP and BRB80. This was incubated for further 3 minutes on ice and then 37 °C glycerol was added to a final percentage of 33 (v/v) % and incubated at 37 °C for 30 minutes. After this polymerisation step the sample was spun on top of a 37 °C low pH cushion at 400000 xg for 25 minutes. The supernatant was removed and the cushion was rinsed twice with 37 °C BRB80. Afterwards the cushion was removed, and the pellet was resuspended in 4 °C BRB80 and incubated on ice for another 30 minutes. The sample was spun a final time at 125000 xg for 10 minutes at 4 °C. The supernatant was collected and the concentration was determined. The concentration was adjusted to 200 µM with 4 °C BRB80, and the labelled tubulin was frozen and stored at -150 °C until further use.

4.3.10 Fluorescence-dye labelling of proteins via sortagging

The N-terminal labelling of proteins was performed by sortagging[95], for which an anorganic dye was conjugated to a small peptide with the sequence LPETGG as described in the next section (4.3.10.1). The labelling reaction was facilitated by recombinant Sortase A from *S. aureus*. Proteins intended for labelling with this method were designed to contain an N-terminal penta-Glycine motive (marked with "Gly-" in section 4.1.4)

For the reaction, the following sample was prepared in a total volume of 0.5 mL:

100-300 µM target protein
1:3-fold µM Sortase A
8-fold excess conjugated LEPTGG
50 mM Tris pH 8
150 mM KCl
6 mM $CaCl_2$
0.5 mM TCEP

Protein specific modifications:
20 % Glycerol (for reactions with SspBAuroraB)
Saturating concentration of flavin mononucleotide (for reactions with iLID)

The sample was incubated at 4 °C overnight. After incubation, the sample was spun for 10 minutes at 14000 xg to remove formed aggregates before SEC. The labelled protein was separated from unlabelled protein and unreacted LEPTGG peptide by SEC using a XK 10/300 Superdex 75 p.g. column. The column was equilibrated in the appropriate SEC buffer for each protein (4.3.6, SEC buffer). The labelled protein was pooled based on the absorption of the conjugated dye and verified by SDS-PAGE (4.4.1). The protein was concentrated with an Amicon Ultra Concentrator or in case of AuroraB with an Amicon Stirred Cell. The concentration was measured by the absorption at 280 nm and corrected for the conjugated dye. The protein was aliquoted, frozen, and stored at -80 °C until further use.

Proteins were labelled with the dyes according to Tab. 7.

Table 7 Protein dyes used for protein labelling

Target protein	**Dye**
SspB-AuroraB	Atto542
iLID	Alexa488
Stathmin	Atto532

4.3.10.1 Peptide-dye conjugation for sortagging

To prepare the dye-conjugated LEPTGG peptide, dyes with an NHS functionalized group were used (NHS-Alexa488, NHS-Atto532 and -542). The dye was solved in DMSO to achieve a concentration of 60 mM, and the LEPTGG peptide was diluted to 40 mM. Equal volumes of dye and peptide were mixed from these solutions, and 20 mM triethylamine were added. The reaction was incubated at 30 °C overnight. The reaction was stopped by addition of 90 mM Tris pH 8. This yielded an 18.18 mM dye conjugated LEPTGG solution which was used during sortagging.

4.3.11 Fluorescence-dye labelling of proteins with maleimide

Maleimide labelling was performed following manufacturer protocols and was only performed to label the stathmin sensor COPY^0 with Atto647. The labelling could be performed before or after sortagging with the donor dye. The labelled protein was separated with the same steps as used for sortagging.

4.4 Bioanalytical methods

4.4.1 SDS-PAGE

SDS-page was performed following the Laemmli method using gels 12.5 % for proteins smaller than 100 kDa, and 10 % gels for proteins bigger than 100 kDa. The electrophoresis was conducted for 30-45 minutes at 50 mA. After the electrophoresis, the SDS-buffer was rinsed of, by washing the gel three times with distilled water. The proteins were fixed in the gel with fixing solution for 15 minutes and stained afterwards with staining solution overnight. Unspecific bound dye was washed out with distilled water for until protein bands were visible.

Collection gel: 125 mM Tris pH 6.8, 4 % acrylamide, 0.4 % SDS, 0.1 % (w/v) APS, 0.075 % (w/v) TEMED

Separation gel: 375 mM Tris pH 8.8, 12.5 or 10 % acrylamide, 0.4 % SDS, 0.1 % (w/v) APS, 0.075 % (w/v) TEMED

Running buffer: 25 mM Tris, 1g/L SDS, 14.4 g/L glycine

2x Sample buffer: 50 mM Tris pH 6.8, 40 % Glycerol, 4 % (w/v) SDS, 15 % β-ME, 18 mg/L bromophenol blue

Fixing solution: 40 % (v/v) Ethanol, 10 % (v/v) acetic acid

Staining solution: 19 mM HCl, 35 mg/L Coomassie Brilliant Blue G-250, 35 mg/L Coomassie Brilliant Blue R-250

4.4.2 Bradford protein assay

For the concentration determination with Bradford, a commercial Bradford reagent (Sigma-Aldrich) was used with a total volume of 700 µL. The protein concentration was kept between 1-15 µg/mL. The reaction was incubated in the dark at room temperature for 10 minutes prior to measuring the extinction at 595 nm. The protein concentration was calculated using a BSA standard curve.

4.4.3 BCA assay

For the concentration determination with bicinchoninic acid, a commercial Micro BCA™ protein assay reagent kit (Thermo Fisher Scientific) was used following the manufacturer's protocol. The protein concentration was kept between 1-15 µg/mL. The protein concentration was calculated with a BSA standard curve.

4.4.4 Spectrophotometric determination of protein concentration

For the concentration determination of proteins, Lambert-Beer's law was applied. This was used for all proteins labelled with inorganic dyes. The absorption of the protein sample was taken at 280 nm and the respective maximum absorption of the dye. The protein was usually diluted 1:10. The predicted extinction coefficient of the proteins was calculated by the ProtParam tool (Expasy), and the coefficient and correction factor of the dye was taken from the manufacturer (Atto-tec/Thermo Fisher Scientific).

4.4.5 MALDI-MS

Successful *in vitro* prenylation of Gly-iLID-tRac1 was verified using a sinapinic acid matrix. The sample was desalted and dilutions of 1:10, 1:100 and 1:1000 were prepared in distilled water. A 1:1 dilution of matrix and the diluted protein was applied to the sample plate and dried. The samples were measured with a MALDI-TOF/TOF UltrafleXtreme Smartbeam spectrometer (Bruker).

4.5 Preparation of liposomes and lipid handling

4.5.1 Electro-formation of liposomes

Generation of GUVs was performed with electro-formation. For this, a 1 mg/mL Lipid in chloroform solution was prepared (see Tab. 8). 20 µL of the solution were applied onto a platinum wire encased in a PTFE chamber. After application, residual chloroform was removed under vacuum for 15 minutes. The chamber was filled with a 450 mM sucrose solution and GUV swelling was induced by applying 2.4 V at 10 Hz to the chamber. After 1 hour of swelling the GUVs were shed from the platinum wire into the sucrose solution by reducing the frequency to 2 Hz for 15 minutes. The GUV-sucrose solution was collected and used for the experiments. The lipid composition was adapted following Tab. 8 if a lipid label was desired for an experiment.

Table 8 Lipid composition

Lipid	**Percentage in mixture**
DOPC	79.9-79.95 % (depending on use of labelled lipid)
DOPS	20 %
Biotinyl-PE	0.05 %
Lissamine-Rhodamine-PE	0.05 % (for experiments with labelled lipids only)

4.5.2 Immobilization of GUVs

To minimize the movement of GUVs during the measurements, the surface of the imaging slide was functionalized with avidin. For this, the surface was first incubated with 1 mg/mL biotinylated BSA in water for 60 minutes followed by further passivation with a mix of 5 mg/mL Casein and BSA in water for 30 minutes. After this, 0.1 mg/mL Avidin in BRB80 buffer (80 mM PIPES pH 6.8, 1 mM $MgCl_2$, 0.2 mM EGTA) was incubated for 60 minutes to finalize the functionalisation. Each step was performed at room temperature and between each step the slide was washed 3 times with water or BRB80 buffer (4.3.8).

4.5.3 Determination of buffer osmolarity

To reduce the destruction of vesicles by osmotic pressure, the buffers used were adjusted to similar osmolarities. For this, the osmolarity of the buffers weas measured using a freezing-point depression osmometer (Knauer, Berlin). For the measurement, 150 µL of buffer was prepared and the measurement was performed following the manufacturer's protocol. If a large difference between inner and outer buffer was measured, the osmolarity was adjusted with sucrose or glucose respectively. The usual osmolarity used was 550 mOsm for inner buffer, which equates to 450 mM Sucrose, and 600 mOsm for outer buffer.

4.6 Preparation of short GMPCPP stabilised microtubule seeds

MT-seeds were prepared by mixing 40 µM tubulin (1:1 ratio labelled to unlabelled tubulin or only unlabelled tubulin) in BRB80 buffer (4.3.8) with 1 mM GMPCPP (Jena Bioscience) and 5 mM β-mercaptoethanol. The mix was incubated at 37 °C for 5 minutes. This short time allowed for small MT-seeds to be generated. After the incubation 400 µL of 37 °C BRB80 (4.3.8) was added to the reaction mix, which was then spun down for 8 minutes at 21.000 xg at room temperature. The supernatant was removed, and the pellet was resuspended in BRB80 and kept at room temperature and was used in experiments on the same day.

4.7 Confocal laser scanning microscopy

All microscopy measurements were performed using a Leica SP8 microscope (Leica Mirosystems). The pixel depth was 16 bit. Depending on the zoom factor used, the pixel field was adjusted to a resolution of less than 0.2 µm/pixel. As objective a 63x/1.2 NA water immersion objective was used. For most experiments, the pinhole was set to 1 Airy with the exception of measurements with COPY^{o} in ILVs where it was set to 3 Airy for the excitation wavelength. In general, the imaging was performed at 37 °C. The line scanning speed was 400 Hz. For measurements without COPY^{o} the scanning speed was 8000 Hz using a resonance scanner.

For excitation of the fluorescent labels, a white light laser was used. The power of the laser was set to 70 % and an intensity of 1-2 % was used for the individual laser lines (Tab. 9).

Table 9 Excitationwave length, laser intensities, and detection windows for confocal microscopy

Fluorescence label	**Excitation wavelength (nm)**	**Laser intensity (%)**	**Emission detection window (nm)**
Alexa488, simultaneous with iLID activation	495	1	505 – 535
EGFP	488	2	500 – 530
Lissamine-Rhodamine	562	2	572 – 602
Atto532 (COPY^{o})	532	50	542 – 572
Atto542	542	1	552 – 582
Atto647 (COPY^{o})	650	Sensitized emission	660 – 750
Alexa647	650	1	660 – 690

The fluorescence emission was detected using hybrid detectors in photon counting mode.

To prevent bleed through, activation and detection of the different fluorescence labels used, scans were performed in a sequential manner using only one laser line per sequence. To reduce movement effects within the samples, the sequences were taken by lines rather than a whole frame at a time.

In general, three kinds of images were taken: (i) single z-plane images, (ii) time series at a single z-plane and (iii) z-stacks of full GUVs.

For time series measurements, specifically used for capturing dynamics of synMMS, images were taken every 4 seconds over a time interval of 5 minutes without activation of the signalling system and 15 minutes with activation. For those measurement, the z-plane had to be adjusted during the time series to keep the observed ILV in focus. For measurements in bulk, mainly for activity checks of SspB-AuroraB, images were taken every 10 seconds for up to 60 minutes.

Z-stacks were usually taken with 1 or 0.36 µm distance between planes. They were mainly taken for measurements where MT-organisation was evaluated, but also for the initial experiments with encapsulation of EGFP.

4.8 Image processing of tubulin images

The resolution of MT-bundles was limited by the high background fluorescence signal of free tubulin. To increase the visibility of MT-bundles in respect to the background of Alexa647-tubulin, the images were therefore enhanced with multiple steps of image processing in ImageJ[70].

First a histogram equalization was performed to enhance the contrast within the image ("Enhance Contrast", 0.3% of saturated pixels). In the next step, two successive directional filters were applied to connect disconnected regions for short and long distances (MorphoLibJ library, Type = Max, Operation = Mean, Direction = 32, Line = 3 and Line = 20, respectively). Due to edge effects occurring after directional filtering, an unsharp mask with a radius of 5 pixels and a mask weight of 0.5 was applied to the images to sharpen the contrast on edges of structures. In a last step, the pixel values of the image were weighted to the intensity of the raw image by multiplication of the processed image with the raw data.

4.9 Analysis of iLID membrane densities

GUVs and ILVs were measured with Confocal Laser Scanning Microscopy at their equator. Defined protein concentrations, indicated for each experiment, were added to immobilized GUVs prior to ehESCRT-III encapsulation. The protein concentration in the bulk was used to calculate the protein densities on the membrane inside ILVs and outside GUVs using a semi-automated tool in Matlab[96].

4.10 Quantification of SspB-AuroraB membrane translocation

To calculated the lumen corrected membrane translocation of Atto542-SspB-AuroraB, first a binary mask of the Alexa488-iLID fluorescence channel was created first by thresholding in ImageJ. The pixels corresponding to the membrane were defined as those 7 pixels away from the edge of the mask. This was obtained by eroding the mask by 7 pixels. Since the optical resolution was ~250 nm, as compared to the ~4 nm width of a lipid membrane, the fluorescence signal at pixels, which include part of the membrane contain contributions from both luminal as well as membrane located SspB-AuroraB. With the membrane marked by Alexa488-iLID the corrected membrane translocation was calculated as

$$R^2 = \frac{AuB_{memb} - AuB_{lum}}{AuB_{memb}}$$

With R^2 being the normalized SspB-AuroraB membrane translocation factor, AuB_{memb} being the fluorescence proximal to the liposome membrane and AuB_{lum} being the fluorescence in the lumen. This analysis was performed on a pixel basis with a custom written code in MatLab 2019b.

4.11 Analysis of the COPY^o phosphorylation gradient

Images for the gradient measurement were acquired as described in section 4.7. Any xy-movement of GUVs and ILVs were corrected separately in ImageJ using the MultiStackReg plugin based on SteckReg[97–99]. Images with significant z-movement of the GUVs or ILVs were excluded.

On average, the sum of 40 registered frames was taken and dark counts were thresholded out. The FRET ratio images (acceptor/donor) were calculated and radial profiles were extracted from the ratio images by a custom macro in ImageJ.

5. Results

5.1 Purification of the ehESCRT-III complex

The encapsulation of reconstituted systems inside of liposomes has been an important subject for the field of synthetic biology, as it is necessary to mimic and establish a boundary between extra- and intercellular spaces for reconstituted proto-cells. Most encapsulation methods to generate reconstituted proto-cells are based on microfluidic devices[100,101].

In an attempt to establish an encapsulation method, inspiration was taken from one of the naturally occurring scission machineries in cells. The ESCRT complex facilitates multiple scission events in different cellular contexts and, if taken out of a cellular context the main scission machinery ESCRT-III still facilitates scission.

Out of the discovered ESCRT-III homologues, the complex from the amoeba *entamoeba histolytica*[102,103] was chosen for this work. To use the complex in a reconstituted manner, a purification pipeline for the individual ESCRT-III components (ehVps20, ehVps32, ehVps24 and ehVps2) was developed. EhVps20 has an inhibitory N-terminal domain, as also shown for homologues in human and yeast[104], which reduces membrane binding without the presence of components from ESCRT-II. For this reason, a deletion construct named ehVps20dC, which only includes the amino acid sequence from residue 1-173.

All four ESCRT-III subunits were cloned into a vector containing a C-terminal MBP-tag to increase solubility of the units. Due to similar behaviour of the individual subunits during purification, all could be purified within the same pipeline:

1. *E. coli* cells were lysed and the lysate was separated in solid and soluble components.
2. The supernatant was cycled over an MBPtrap™ column for 2-3 hours and after extensive washing with buffer the MBP-tagged subunit was eluted with 20 mM maltose.
3. Eluted protein was further purified to remove maltose and other impurities by SEC using a Superdex 200 column, and afterwards the MBP-tag was removed by TEV digestion overnight.
4. After the incubation, TEV and MBP-tag were removed by affinity chromatography on a HisTrap™ column with 20 mM Imidazole to suppress unspecific binding of ESCRT-III subunits but retaining the binding of the His6-tag on MBP and TEV.

5. In a final step, the ESCRT-III subunit was further purification by SEC using a Superdex 75 column.
6. ehVps20dC, ehVps24 and ehVps2 were concentrated up to 50 µM, whereas ehVps32 was only concentrated up to 10 µM. These concentration limits were important due to the formation of aggregates at higher concentrations.

With this purification pipeline, a successful purification of each ESCRT-III subunit was feasible.

5.2 Encapsulation using the ehESCRT-III complex

5.2.1 Establishment of a protein-based encapsulation assay

The reconstituted functionality of the minimal scission machinery of ESCRT-III has been shown with yeast[35] and human homologues[105] on GUVs with a similar charge to membranes found in living organisms (~20% negative charge), due to the property of ESCRT-III to bind to negatively charged membranes.

To first demonstrate that the ESCRT-III homologues from *entamoeba histolytica* function in a reconstituted system, encapsulation assays inspired by the work of Wollert et. al 2009[35] were performed.

For the encapsulation assay, GUVs with 20% negative charge were generated (4.5) and mixed with BRB80 buffer. The osmolarities of the buffers were adjusted with glucose to generate a hyper-osmotic pressure of 50 mOsm. This difference in osmolarity induces small membrane fluctuation and thereby causes spontaneous membrane curvature, which increases binding of ESCRT-III proteins[106]. To distinguish ILVs formed during GUV generation from ILVs encapsulated by ehESCRT-III 10 µM Strep-EGFP was used as a bulk marker. The ehESCRT-III subunits were added sequentially with a five-minute incubation period between each subunit addition. To compensate for high lipid content in the assay, the protein concentrations were increased compared to previously published results with homologue ESCRT-III complexes[35].

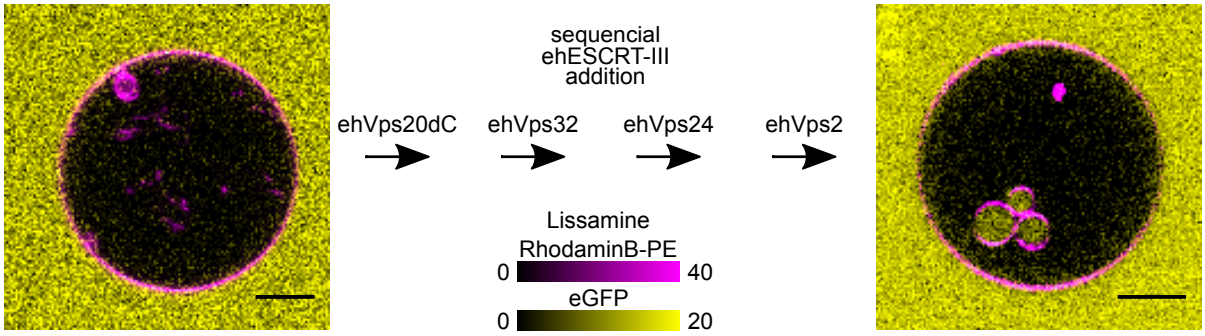

Figure 8 Encapsulation of EGFP using ehESCRT-III. CLSM image of a GUV in 10 µM EGFP (yellow) solution with ILVs formed after encapsulation. Membrane labelled with LissamineRhodamineB-PE (magenta). Scalebars 10 µm.

First, 600 nM ehVps20dC was added sequentially followed by 1200 nM ehVps32, 300 nM ehVps24 and 300 nM ehVps2. Between each addition, the assay mix was incubated for at least 5 minutes at 37 °C. Tracking GUVs after each incubation, while EGFP was present as a bulk fluorescence marker, the stepwise generation if ILVs inside of the mother GUV could be demonstrated (Fig. 8).

This experiment demonstrates that not every GUV observed formed ILVs upon incubation with the complex. To further assess this, the number of GUVs containing ILVs before and after ESCRT-III complex encapsulation was quantified.

5.2.2 Encapsulation parameters of ILVs generated with ehESCRT-III

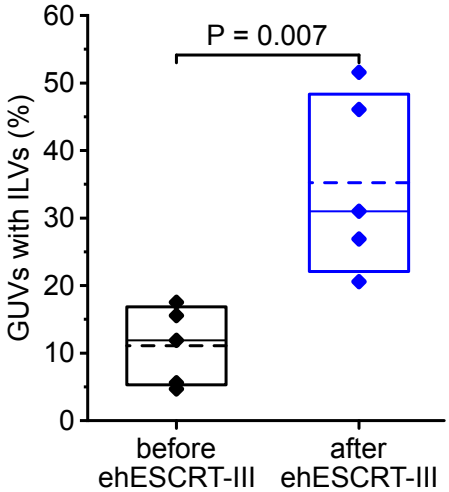

Figure 9 GUVs containing ILVs before and after ehESCRT-III addition. Box: standard deviation; dashed line: mean, line: median. diamond: data points (N=5 individual experiments with n>200 GUVs). p-values from paired Kolmogorov-Smirnov test with 95% confidence interval.

The ILV formation was measured by evaluating GUVs that contained ILVs with EGFP fluorescence before and after addition of the complex. Before the addition of ehESCRT-III, an

average of 11.1 ± 5.8 % GUVs showed ILVs containing EGFP signal. This encapsulation derives from ILVs formed during the generation of the GUVs with electro-formation, which are or were connected to the bulk solution after EGFP was added. After addition of the ehESCRT-III complex, the fraction of GUVs with ILVs containing EGFP fluorescence increased to 35.2 ± 13.1 % (Fig. 9).

These results demonstrate that the ehESCRT-III still functions as an encapsulation/scission machinery in a reconstituted system, similar to its homologues from yeast and human.

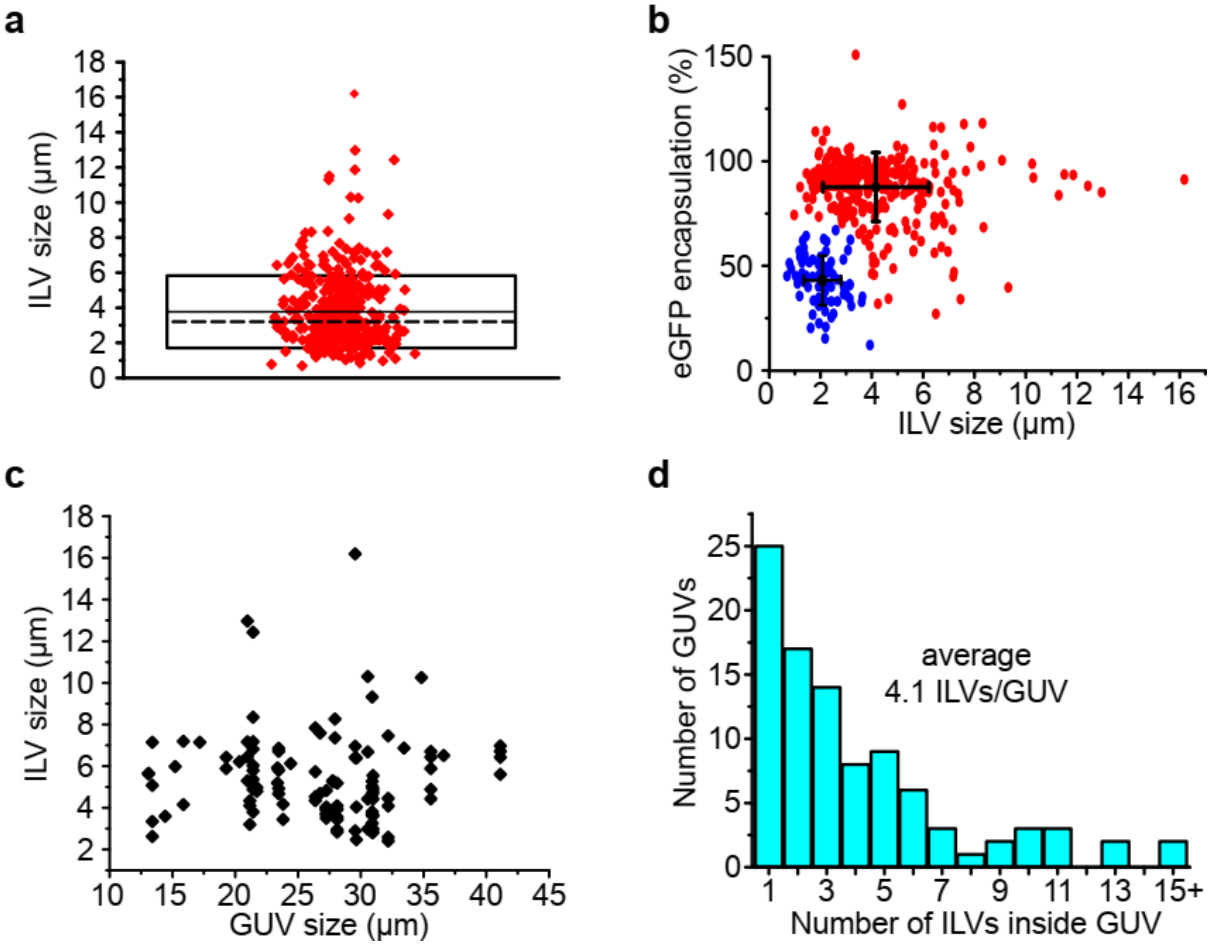

Figure 10 Parameters of ILVs generated by ehESCRT-III. (a) Size distribution of ILVs formed. Box: standard deviation; dashed line: mean, line: median. diamond: data points (n=396 ILVs). (b) Encapsulation efficiency of 10 µM EGFP depends on ILVs size (n=396 ILVs). Black diamond and square mark mean of the cluster, whiskers show standard deviation. (c) ILV size vs. dependence to GUV size. (n=93 GUVs) (d) Distribution of number of ILVs formed per GUV (n=93 GUVs).

Furthermore, the size of ILVs generated after the encapsulation with ESCRT-III (Fig. 10a) was measured. On average, the ILVs were 3.77 ± 2.06 µm in diameter.

Strikingly, by plotting the encapsulation efficiency, calculated by dividing the fluorescence intensity between the bulk surrounding the GUVs and the ILVs lumen, against the size of the ILVs two clusters could be distinguished (Fig. 10b). On cluster displayed a tendency of smaller ILVs with low encapsulation efficiency (red cluster), whereas the other cluster contained

bigger ILVs with high encapsulation efficiency (blue cluster). The lower cluster averages an ILV size of 2.07 ± 0.73 µm and an encapsulation of 43 ± 12 %, whereas the higher cluster averages an ILV size of 4.15 ± 2.07 µm and an encapsulation efficiency of 88 ± 17 %. Most likely the cause for the blue cluster exhibiting lower encapsulation efficiencies is a limitation of the imaging, based on the point spread function of the microscope. For small ILVs, the point spread function is bigger than the ILV itself and the detection integrates not only the fluorescence signal of the ILVs lumen but also the absence of fluorescence signal from the lumen of the GUV the ILV resides in. This in general leads to a lower fluorescence intensity in smaller ILVs.

Interestingly, the size of ILVs was independent of the size of the GUV they formed in (Fig. 10c) with the logical exception of ILVs not exceeding the size of the GUV they are formed in.

Furthermore, the number of ILVs formed within a single mother GUV (Fig. 10d) was quantified. In the majority of cases, only a few 1-3 ILVs were formed inside a GUV, whereas more than 10 ILVs occurred only in a hand full of GUVs. This led on average to 4.1 ILVs being formed within one GUV. Additionally, if a high number of ILVs were formed in a GUV, the ILVs mostly were smaller than average.

5.3 Encapsulation of a MT-cytoskeleton

The encapsulation of a dynamic cytoskeleton, within liposomes has been of significant interest as a stepping stone on the way to a synthetic proto-cell, as e.g., MTs are relevant for numerous cellular processes. It has been shown in previous work that a centrally organized MT system can be encapsulated and exhibit fundamental dynamic features, like self-induced capture and self-organization[70].

To demonstrate that the ESCRT-III complex preserves protein functionality tubulin was encapsulated at low temperatures (4 °C) where MT-dynamics are dominated by the catastrophe frequency. Furthermore, all experiments in this chapter were performed with 2 mM GTP as energy source for tubulin.

To compensate for slower reaction rates at lower temperatures, the incubation step between the addition of the ehESCRT-III components was increased to 15 minutes each. After the incubation, the sample was heated to 37 °C to induce MT-polymerisation. This adaptation to the encapsulation process was used for all measurements with tubulin. To increase the

visibility of MTs against the background fluorescence of unpolymerized tubulin, image enhancement was performed (4.8) as developed in previous work[70].

5.3.1 Tubulin encapsulation

To demonstrate that tubulin preserves its capability to polymerize during the encapsulation with ehESCRT-III, 50 µM tubulin was encapsulated into ILVs. For detection of tubulin, a trace amount of 5 % tubulin labelled with Alexa647 was added.

After the last incubation, the sample were transferred to 37 °C to facilitate tubulin MT-nucleation and polymerization. After the sample reached 37 °C, a MT-mesh could be observed in the bulk around the GUVs (Fig. 11a).

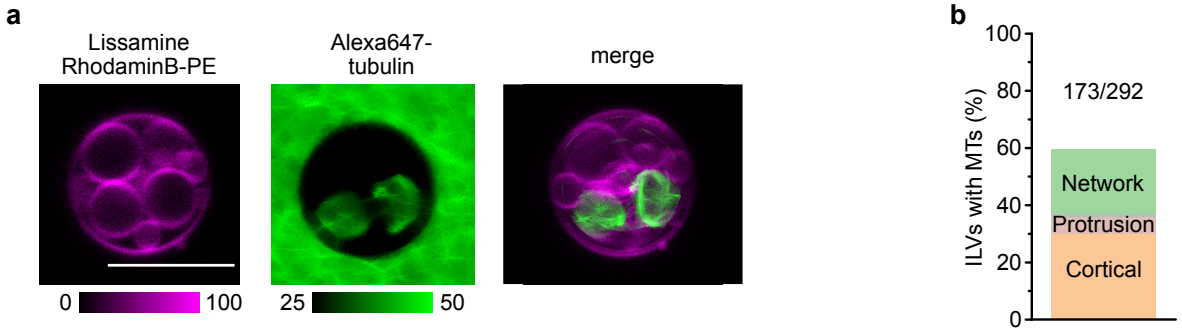

Figure 11 Encapsulation of tubulin into ILVs. (a) Maximum intensity projection of a representative GUV with ILVs with 50 µM Alexa-647-tubulin (green) and Lissamine-RhodamineB-PE (magenta). Bulk fluorescence was masked out for the merge. (b) MT-formation inside ILVs categorized by MT-organization. Cortical MTs (orange) and MT-mesh (green) show a portion of ILVs with protrusion (overlay).

The high fluorescence signal of MTs in the mesh in the bulk made a direct measurement of the encapsulation efficiency of tubulin problematic. To circumvent this issue, the fraction of ILVs that displayed clear MT-structures within ILVs were analysed (Fig. 11b). This resulted in 59.3 % of ILVs with MT-structures inside. 40.7 % of ILVs showed tubulin fluorescence but no clear MT-structures. The MT-structures could be classified into two categories: one being a mesh with MTs spanning the lumen of the ILVs, and cortical, with MTs forming MT-bundles close to the membrane, spanning the whole ILV. The majority of ILVs with tubulin showed a cortical MTs (35.9 %), while and 23.6 % showed a MT-mesh. A minor subcategory of ILVs with MT-structures furthermore showed protrusions originating from them. This fraction was a total of 6.8 % with 5.8 % originating from cortical MTs and 1 % originating from the MT-mesh (Fig. 11b).

After an extended period of time, the MT-structures collapsed around the GUVs and within the ILVs due to degradation of the proteins as well as continued consumption of the GTP energy source.

These results demonstrate that the polymerisation of tubulin to MTs in ILVs formed with the ESCRT-III complex is not impeded. However, the high fraction of ILVs without any polymerized MTs after encapsulation further indicated that the encapsulation efficiency of tubulin played a significant role for MT-polymerization within ILVs.

5.3.2 Tubulin encapsulation with an MTOC

In cells, MT-structures rarely nucleate on their own but generally originate from a MTOC, mostly the centrosome, which also acts as a nucleation centre for the initialisation of MT-polymerisation. In an initial effort to encapsulate an MTOC, the encapsulation of purified centrosomes was tested, which have been used for previous work[70]. In multiple experiments this yielded no encapsulation of centrosomes within ILVs formed with the ESCRT-III complex. The conclusion from these experiments was that the purified centrosomes first and foremost were too diluted and thereby the probability of the centrosome meeting the neck formed before scission was very low. Upon further literature search, a secondary factor emerged that further supported the notion, that centrosomes could not be encapsulated with ESCRT-III. The size of the lipid neck formed by the ESCRT-III complex during the encapsulation process was reported to be smaller than the centrosome. This was additionally supported by the observations that the purified centrosomes rarely were found individually but rather as multicentrosomal clusters.

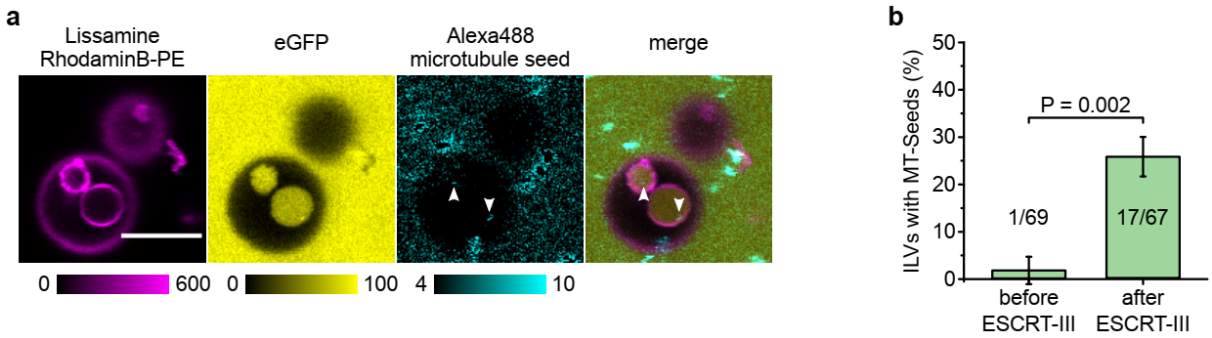

Figure 12 Encapsulation of GMPCPP-stabilized MT-seeds. (a) CLSM image of GMPCPP stabilized MT-seeds labelled with Alexa488 (cyan) co-encapsulated with 10 µM EGPF (yellow) into Lissamine-RhodamineB labelled ILVs (magenta). Arrowheads mark MT-seeds, scalebar 10 µm. (b) MT-seed incorporation into ILVs before and after ehESCRT-III mediated encapsulation (N=3 individual experiments n>20 GUVs, whiskers: SD). p-values from paired Kolmogorov-Smirnov test with 95% confidence interval.

Based on this finding, it was investigated if a smaller MTOC could be encapsulated with the ESCRT-III machinery. As a target for this, GMPCPP-stabilized MT-seeds were chosen, which can easily be created and labelled (4.6). Furthermore, the MT-seeds have identical dimensions to normal MTs, which would theoretically fit through the encapsulation neck (50 nm neck size, 24 nm MT-seed diameter). To see if small MT-seeds could be encapsulated with the ESCRT-III complex, MT-seeds labelled with a fraction of Alexa488 tubulin along with 10 µM of EGFP as a bulk marker (Fig. 12a), to identify ILVs formed during the encapsulation reaction, were encapsulated.

To quantify the encapsulation efficiency of the MT-seeds, ILVs with EGFP fluorescence before and after ESCRT-III addition were counted and the number of ILVs that also had at least one MT-seed incorporated was assessed. Before the addition of the complex, only 2.9 ± 1.7 % of ILVs contained an MT-seed, which is likely caused by ILVs formed during vesicle generation that are still connected at the time the MT-seeds were added. After ESCRT-III addition the encapsulation efficiency drastically increased to 25.6 ± 4.2 % (Fig. 12b).

This result demonstrates that the encapsulation of a simple MTOC like an MT-seed is possible. The rather low encapsulation efficiency also points to the fact, that the passing of the encapsulation neck by the big MT-seed compared to simple monomeric bulk proteins is les probable. While the diameter of the MT-seed fits through the encapsulation neck, the length of the structure makes the processes during encapsulation homologous to threading a needle.

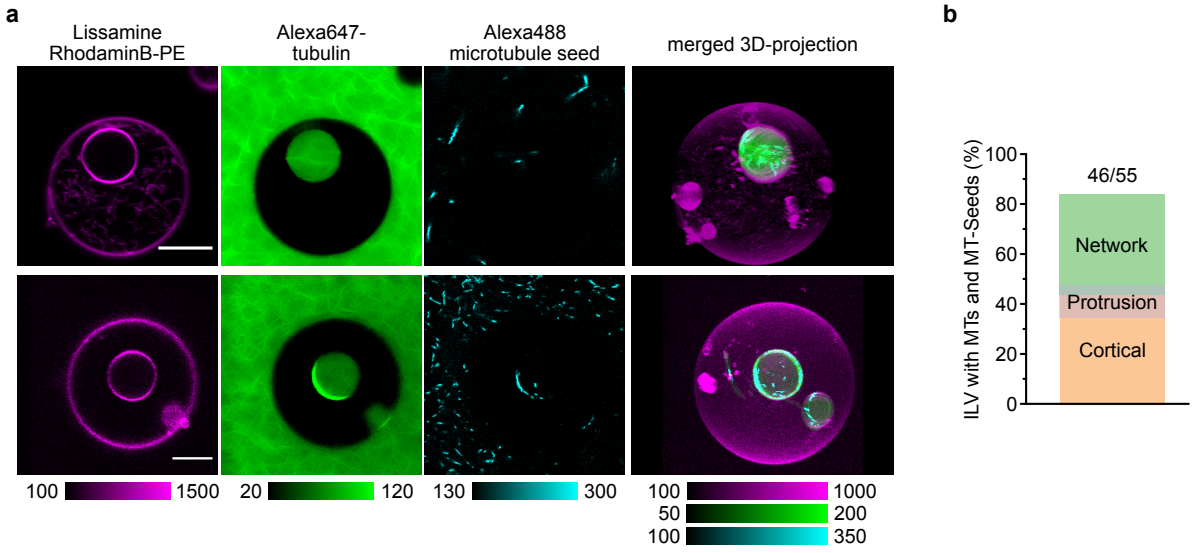

Figure 13 Encapsulation of soluble tubulin with GMPCPP stabilized MT-seeds. (a) Exemplary CLSM images of MT-seeds (cyan) with 30 µM Alexa647-tubulin (green) in ILVs labelled with Lissamine-RhodaminB-PE (magenta) and Merged 3D-projection of the images with bulk fluorescence masked out. Scalebar 10 µm. (b) MT-formation inside ILVs categorized by MT-organization. Cortical MTs (orange) and MT-mesh (green) show a portion of ILVs with protrusion (overlay).

Going back to the results that only about 60 % of ILVs form MT-structures when encapsulating tubulin alone (5.3.1), it was investigated if the fraction of ILVs with MT-structures would be increased when MT-seeds were incorporated as nucleation sites. For this, Alexa488 labelled MT-seeds were encapsulated together with 30 µM tubulin with 5 % Alexa647 labelled tubulin as fluorescent tracer (Fig. 13a). The encapsulation reaction was executed as for the measurement with tubulin alone.

To judge the fraction of ILVs with MT-structures in the presence of MT-seeds, only ILVs that contained MT-seeds were taken into consideration. This demonstrated that 83.9 % of ILVs observed contained MT-structures (Fig. 13b) which is a 20 % increase from tubulin alone despite the lower concentration of tubulin in the experiments. Additionally, the formation of a dense MT-mesh with incorporated MT-seeds around the GUVs could be observed.

Furthermore, the MT-structures formed within the ILVs were classified into the same classes as for tubulin alone. This resulted in 43.6 % of ILVs with cortical MTs and 40 % of ILVs with a MT-mesh. 12.7 % of the 83.9 % of ILVs with MT-structures also showed protrusions (Fig. 13a, lower merged 3D projection) with 9.1 % originating from cortical MTs and 3.6 % originating from an MT-mesh. Furthermore, in most ILVs that formed protrusions a MT-seed was present within the protrusion itself (Fig. 13a, lower merged 3D projection).

With these results it could be demonstrated, that it is possible to encapsulate small MTOCs into ILVs with the ESCRT-III complex. The factor that restricts the encapsulation is predominantly the size of the complex to encapsulate, which needs to be compatible with the size of the membrane neck formed during the encapsulation. The major downside of encapsulating bigger protein complexes is the fact that only a fraction of ILVs formed during encapsulation contain the complex, which results in a lower sample size per measurement and less observable ILVs in total. This is illustrated by the ~5-fold difference in ILVs observed over a greater number of experiments (tubulin only N = 4, n = 292; tubulin with MT-seeds N = 7, n = 55).

5.3.3 Tubulin encapsulation with nucleation factors

Given the problematic encapsulation of the bigger MTOCs and the relatively low yield of MT-structures with tubulin alone, an alternative to increase the MT-nucleation was necessary. In cells, the MT-dynamics and MT-organizations are not controlled by the MTOC alone but rather

by a complex mix of other protein factors, like nucleation and (de)stabilization factors. Roostalu et. al. established, that combination of the MT polymerase chTOG and the MT-stabilization factor TPX2 increases MT-polymerisation *in vitro*[74].

In a first step it was qualitatively verified that ch-TOG and TPX2 reduce the tubulin concentration required for MT-nucleation and polymerization by titrating tubulin in the presence of 100 nM of both factors at 37 °C. MT-polymerisation was judged by the formation of MTs in bulk. Without ch-TOG and TPX2, MTs could be observed at a tubulin concentration of 25 µM whereas with ch-TOG and TPX2 MTs formed at 20 µM. This demonstrates that ch-TOG and TPX2 indeed increase MT-polymerisation at lower concentrations. Due to the fact that these measurements were conducted with confocal microscopy rather than total internal reflection fluorescence microscopy the concentrations vary from other reported values.

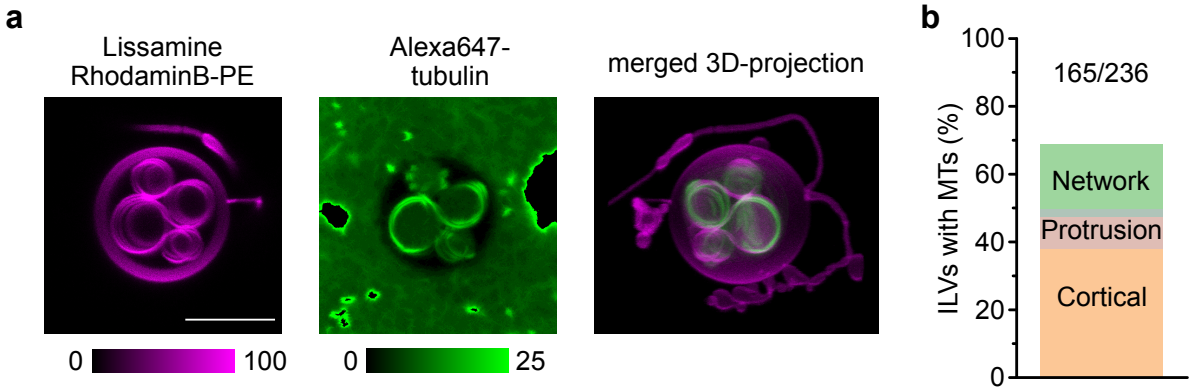

Figure 14 MT-formations in ILVs with tubulin and nucleation factors. (a) 3D-projection of ILVs with 40 µM Alexa647-tubulin (green) and 100 nM of ch-TOG and TPX2. Membrane labelled with Lissamine-RhodamineB (magenta). Large tubulin aggregates were thresholded out, and for the merge the bulk tubulin fluorescence was masked out. Scalebar 10 µm. (b) MT-formation inside ILVs with the conditions as in (a). Cortical MTs (orange) and MT-mesh (green) show a portion of ILVs with protrusion (overlay).

Based on this concentration and to correct for the encapsulation efficiency of tubulin 40 µM tubulin with 100 nM of ch-TOC and TPX2 were used and encapsulated via ESCRT-III into ILVs (Fig. 14a). After encapsulating this protein mixture into ILVs, 67.4 % of the ILVs showed MT-structures inside (Fig. 14b). Of this, 46.2 % of ILVs had cortical MTs and 21.2 % had a MT-mesh. Of these ILVs 14 % also showed a MT-protrusion, 11.4 % originating from cortical MTs and 2.6 % originating from an MT-mesh.

With this, the total amount of ILVs increased by ~10 % with nucleators compared to measurements with tubulin alone them demonstrating, that the inclusion of the ch-TOG and TPX2 increases the formation of MT-structures in ILVs even at a lower concentration of tubulin. Both these proteins are not as effective for the nucleation and polymerisation of

tubulin into MTs as the MT-seeds, which have a ~10 % higher fraction of ILVs with MT-structures. But the total number of ILVs that could be observed was significantly higher (tubulin with ch-TOG and TPX2 N = 7, n =236; ILVs tubulin with MT-seeds N = 7, n = 55), making this variant of the system more viable for further investigation.

5.4 Encapsulation of a biomimetic signalling system

In cells, the cytoskeleton is regulated by a plethora of signalling networks. In previous work, a biomimetic signalling system inspired on the canonical Rac1-PAK1-stathmin MT-regulatory network has been implemented (2.6)[70].

In the following sections, the biomimetic signalling system was built up stepwise and it was demonstrated that its functionality is not affected by the encapsulation into ILVs via the ESCRT-III complex. All experiments with SspB-AuroraB were performed with 2 mM ATP as energy source.

5.4.1 Encapsulation of membrane associated iLID

The encapsulation of membrane associated proteins in liposomes is in general a tedious effort, due to the lipophilic properties of these proteins and the fact that many encapsulation methods use oil phases during the liposome formation.

To demonstrate that the encapsulation with ESCRT-III also works for peripheral membrane proteins rather than only for soluble proteins, it was tried to encapsulated these. For this, our two established ways to locate the photo-activatable iLID to the membrane were chosen. These are the prenylated C-terminus of Rac1 as well as the phosphatidylserine-binding C2 domain from bovine lactadherin, which both associate the protein peripherally to the membrane.

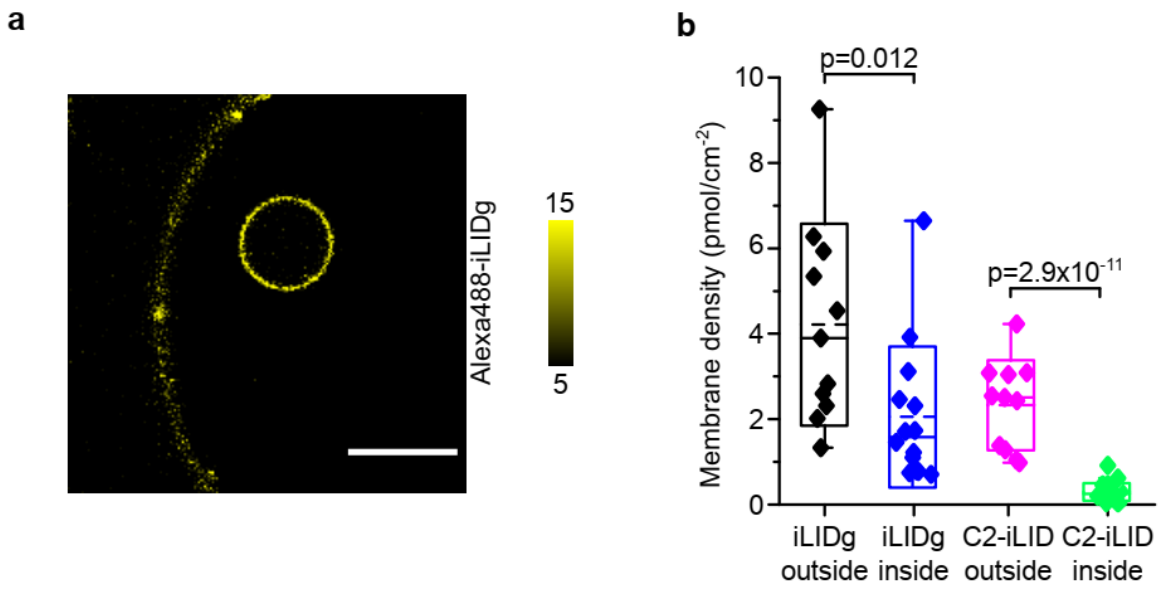

Figure 15 Encapsulation of membrane associated proteins. (a) CLSM image of 10 µM Alexa488-iLIDg on the membrane. Scalebar 10 µM. (b) Membrane density inside ILVs and outside of GUVs for 10 µM Alexa488-iLIDg and 1 µM Alexa488-C2-iLID (black: n=11, blue: n=13, magenta: n=11, green: n=24). Box: standard deviation; dashed line: mean, line: median. diamond: data points, whiskers: 5- and 95%-percentiles. p-values from paired Kolmogorov-Smirnov test with 95% confidence interval.

To demonstrate that membrane associated proteins could be encapsulated, 10 µM of geranylgeranylated iLID (iLIDg, Fig. 15a) or 1 µM of C2-iLID were encapsulated with the same method as described for EGFP (5.2.2). The iLID constructs were labelled with Alexa488. The difference in concentration was necessary due to differences in the membrane affinity of the individual membrane tags. The membrane density (4.10) for both iLID constructs was quantified for the outside of the GUV and for the inside of the ILVs formed during the encapsulation. For both iLID constructs, the membrane density inside the ILVs was lower than outside the GUVs (Fig. 15b, black to blue and magenta to green). On average, iLIDg had a membrane density of 4.2 ± 2.4 pmol/cm^2 outside the GUVs and 2.1 ± 1.6 pmol/cm^2 inside the ILVs, whereas C2-iLID had a membrane density of 2.3 ± 1.0 pmol/cm^2 outside of GUVs and 0.28 ± 0.18 pmol/cm^2 inside of ILVs. Edge effects on the membrane during imaging cannot explain the difference between inside and outside membrane densities for C2-iLID alone, but surely influenced the result of these measurements.

These results reveal that there is a significant difference between the encapsulation efficiency of the two iLID constructs. This difference can be explained partially by the binding of the iLID constructs to the membrane. C2-iLID tightly binds to the negatively charged DOPS lipids and thereby reduces the effective negative charge of the membrane which is needed for the

ESCRT-III complex to associate to the membrane to facilitate the encapsulation reaction. This is not the case for the geranylgeranylated iLIDg, which still associates loosely to the negative charged DOPS by the polybasic motive but more so binds to the membrane by the insertion of the geranylgeranyl-tail into the lipid bilayer.

With this revelation, all further experiments with iLID present were performed with iLIDg due to the better encapsulation efficiency with the ESCRT-III complex.

5.4.2 Encapsulation and validation the optical dimerizer system iLID/SspB

To complete the optical dimerizer system, SspB-AuroraB was encapsulated. For one, this would reveal if other soluble proteins would be encapsulated to the same extent as EGFP as well as prove the functionality of the dimerizer system after encapsulation by observing the light-induced membrane translocation of SspB-AuroraB.

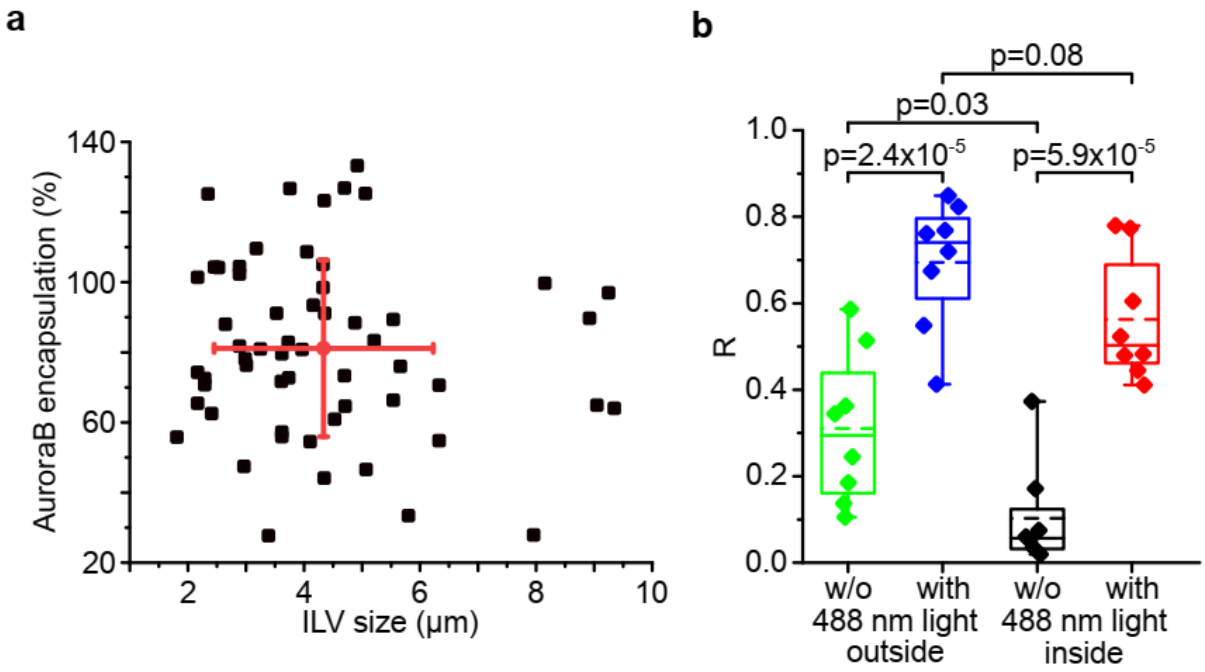

Figure 16 Encapsulation of SspB-AuroraB and membrane translocation to iLIDg. (a) Encapsulation efficiency of 1 µM Atto542-SspB-AuroraB and size distribution of ILVs (n=58). Red diamond indicates the mean and whiskers indicate standard deviation. (b) Lumen-corrected translocation of 1 µM SspB-AuroraB to 10 µM iLIDg to the membrane before and after irradiation with 488 nm light for 5 minutes. Box: standard deviation; dashed line: mean, line: median. diamond: data points whiskers: 5- and 95%-percentiles (N=8 ILVs). p-values from paired Kolmogorov-Smirnov test with 95% confidence interval.

For this, 1 µM SspB-AuroraB, labelled with Atto542, alongside 10 µM Alexa488-labelled iLIDg were encapsulated with the ESCRT-III complex in the same manner as EGFP (5.2.2). Due to the fact, that SspB-Aurora was mainly in bulk before the photo-activation of the dimerizer system with 488 nm light, the encapsulation efficiency was quantified. Interestingly, this encapsulation displayed no obvious subpopulations when plotted against the size of the ILVs (Fig. 16a). The encapsulation efficiency of SspB-AuroraB was on average 81.1 ± 25.2 % while the ILV size averaged at 4.34 ± 1.89 µm. This result was in accord to the initial measurements performed with EGFP.

To prove the functionality of the iLID/SspB system, the translocation of SspB-AuroraB was induced by illuminating the GUV and ILVs for 5 minutes with 488 nm light. The translocation was quantified with the lumen-corrected translocation of SspB-AuroraB, termed R. The correction of the SspB-AuroraB translocation was useful to minimize the contribution of the lumen to the fraction of translocated mass, simply based on the size difference between the width of the membrane (~5 µm) compared to the optical resolution (~250 µm).

Analysed this way, R could be compared before the light-induced translocation (first frame of the activation series), which corresponds to the dark binding within the system, to afterwards (last frame of the activation series) for both the outside of GUVs and the inside of ILVs formed during encapsulation with ESCRT-III (Fig. 16b). For the outside, R before photo-activation was 0.31 ± 0.17 (green), which increased significantly during photo-activation to 0.69 ± 0.14 (blue). For the inside of ILVs, R before activation was 0.1 ± 0.1 (black) and increased significantly to 0.56 ± 0.14 (red).

These results demonstrate that the iLID/SspB system conserved its activity during the encapsulation process. Furthermore, these results indicate that the dark binding of the iLID/SspB system is highly dependent on the available concentration of SspB substrate. This also points towards a depletion of SspB-AuroraB from the lumen inside ILVs which is not present for the outside membrane.

5.4.3 Functional encapsulation of the stathmin phosphorylation gradient measured with COPY^{o}

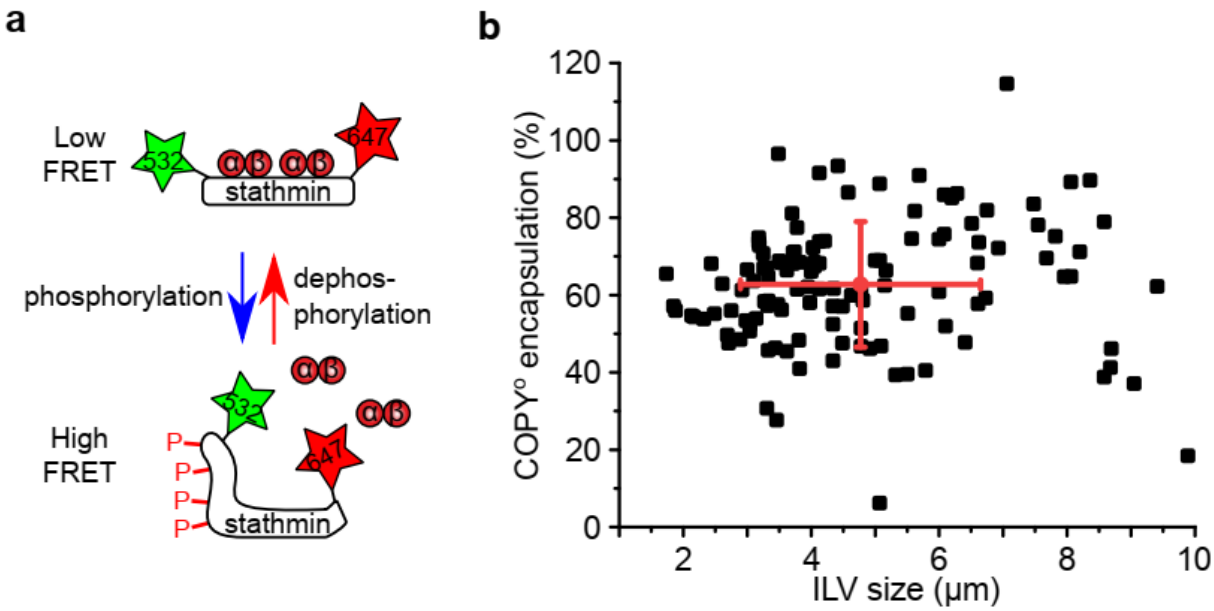

Figure 17 Stathmin phosphorylation sensor COPY^{o}. (a) Scheme of the FRET states of the stathmin sensor COPY^{o}. (b) Encapsulation efficiency of 10 µM COPY^{o} measured by donor fluorescence and size distribution of generated ILVs (n=121).

To couple the photo-activatable signalling system to the cytoskeletal system, the MAP stathmin was utilized to modulate the tubulin concentration and thereby alter MT-polymerisation. To demonstrate the functionality of stathmin's ability to sequester tubulin the stathmin phosphorylation FRET-sensor COPY^{o} (Fig. 17a) was used, which has been characterized in previous work[70]. The sensor was designed with an N-terminally conjugated Atto532 and a C-terminally conjugated Atto647 (see methods). COPY^{o} allows the measurement of the phosphorylation state of stathmin and the binding state of tubulin. The unphosphorylated state binds to two tubulin dimers and has a low FRET signal, whereas the phosphorylated state undergoes a conformational change and loses its binding affinity for one tubulin dimer and thereby has a high FRET signal.

Initially, the encapsulation efficiency of COPY^{o} was measured by encapsulating 10 µM COPY^{o} together with 20 µM tubulin. To reduce tubulin degradation, 40 µM GTP was added to all experiments with the COPY^{o} sensor. This resulted in an encapsulation efficiency of 62.7 ± 16.3 % with an average ILV size of 4.77 ± 1.87 µm (Fig. 17b). While the ILV size was consistent with the results obtained for EGFP and SspB-AuroraB, the encapsulation efficiency was ~20 % lower. This apparently lowered efficiency was likely caused by donor dye (Atto532) quenching through the acceptor dye (Atto647).

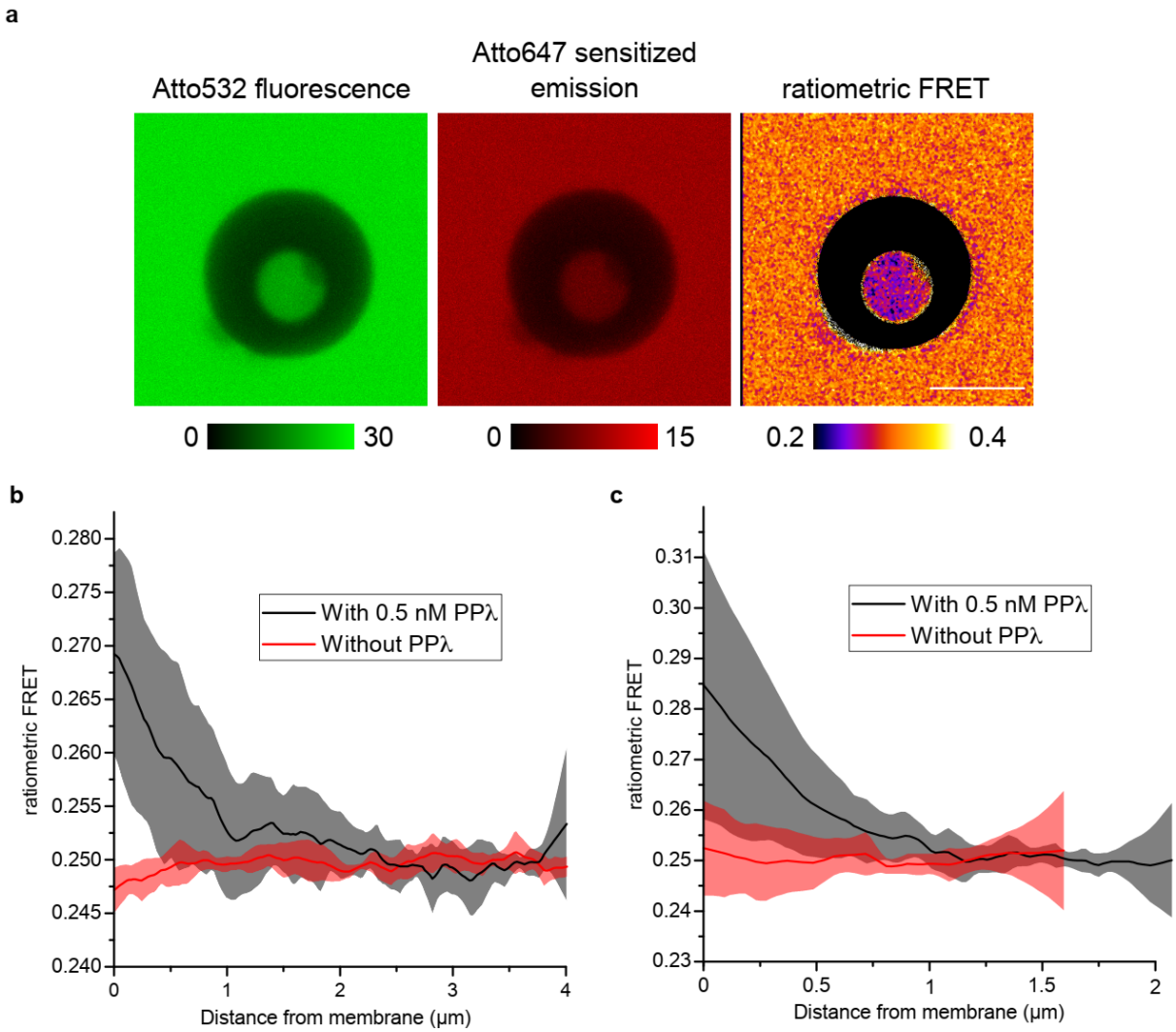

Figure 18 Ratiometric COPY^{o} phosphorylation gradient. (a) Representative summed CLSM images and ratiometric FRET image of 10 µM COPY^{o} after 5 minutes of irradiation with 488 nm light. Scalebar 10 µm. (b) Ratiometric profile of COPY^{o} outside of GUVs with and without 0.5 µM PPλ (Without PPλ: red, n=8, with PPλ: black, n=7). Shaded areas indicate standard deviation. (c) Ratiometric profile of COPY^{o} inside of ILVs with and without 0.5 µM PPλ (Without PPλ: red, n=9, with PPλ: black, n=7).

For the measurement of the stathmin phosphorylation gradient, 10 µM COPY^{o} was encapsulated together with 20 µM tubulin, 10 µM iLIDg, 4.5 µM SspB-AuroraB, 2 mM ATP and with or without 0.5 µM PPλ (estimating a similar encapsulation efficiency as obtained for EGFP and SspB-AuroraB) into ILVs with the ESCRT-III complex under the same conditions as the measurements with the other components of the signalling system. The formation of the gradient was induced by the 488nm light-induced translocation of SspB-AuroraB to iLIDg on the membrane for 5 minutes (Fig. 18a). After 5 minutes of photo-activation, the sample was measured and ratiometrically analysed. To compensate for z-movement of the ILVs inside the GUVs, these measurements were performed using a resonant scanner with 8 kHz and a 3 airy pinhole (more details see 4.7).

In the presence of 0.5 µM PPλ, a phosphorylation gradient of COPY^{o} could be measured outside of GUVs (Fig. 18b, black curve) as well as inside of ILVs (Fig. 18c, black curve). If PPλ was not present in the measurement no phosphorylation gradient of COPY^{o} could be established (Fig. 18b,c, respectively). This indicates that the gradient was dynamically maintained by the (de)phosphorylation cycle facilitated by AuroraB and PPλ. Interestingly, the phosphorylation gradient established inside of ILVs displays a higher amplitude compared to the gradient established outside but it also displays a higher variability between individual curves illustrated by the standard deviation. This higher variability is caused by the curvature difference of the membranes exposed to the protein solution, where the outside membrane has a convex curvature towards the protein solution and the inside has a concave curvature towards the protein solution. This, together with the size difference between the GUVs and ILVs, affects the effective volume of detection during the imaging via confocal microscopy, especially considering with the widened pinhole used for these experiments. Non the less the gradients have a similar decay length of ~0.5 µm from the membrane.

These results were consistent with previous work[70], furthermore, demonstrating that the full biomimetic signalling system is fully functional after the encapsulation into ILVs with the ESCRT-III machinery, with comparable amplitude and decay length of the gradient formed.

5.5 Encapsulation of the synthetic morphogenic membrane system and its behaviour in bulk

With the successful encapsulation of the MT cytoskeleton (5.3) and the biomimetic signalling system (5.4), the encapsulation of both systems combined was investigated. In divergence from previous work with synMMS[70], several adjustments had to be made, with the most important difference being the exclusion of centrosomes as the central MTOC in the system. Besides that, a third detection channel was added to the system. This allowed for the entanglement of SspB-AuroraB translocation and detection, while also leaving space in the spectrum for labelled iLIDg to mark the membrane of the liposomes. Furthermore, the SspB-AuroraB concentration was reduced from 4.5 µM to 2 µM and the concentration of stathmin was reduced from 4 µM to 2 µM. As concluded from the tubulin experiments, with the inability to encapsulate a centrosome and the low overall efficiency of MT-seed encapsulation, the nucleators ch-TOG and TPX2 were included with a concentration of 0.1 µM each. The tubulin concentration was set to 40 µM, while the PPλ was used with a concentration of 0.5 µM. As an energy source, GTP and ATP were used with a concentration of 2 mM.

For these experiments, the encapsulation was performed similarly to the experiments with the cytoskeletal system alone to prevent polymerised MTs to interfere with the encapsulation process. And after the encapsulation reaction the sample was heated to 37 °C before imaging (see methods).

5.5.1 SspB-AuroraB translocation in synMMS and its property as nucleation factor for tubulin

The encapsulation with the ESCRT-III machinery has additional benefits in measurements with synMMS. It allowed, besides the observation of the encapsulated system, the observation of the synMMS system in bulk, which has not been investigated in closer detail to this point.

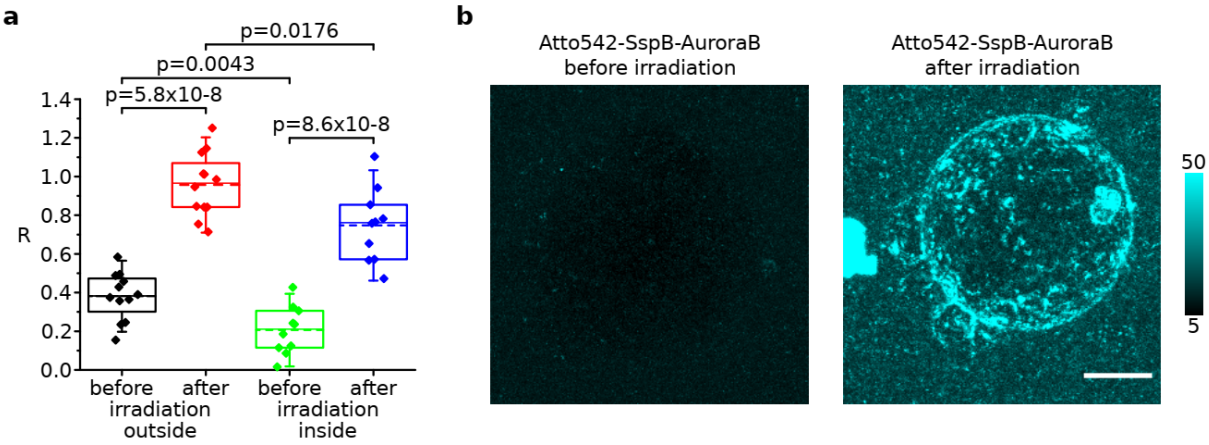

Figure 19 SspB-AuroraB membrane translocation in synMMS. (a) Lumen-corrected translocation of 2 µM SspB-AuroraB to 10 µM iLIDg on the membrane before and after irradiation with 488 nm light for 15 minutes with the full synMMS. Box: standard deviation; dashed line: mean, line: median. diamond: data points whiskers: 5- and 95%-percentiles (N=10 ILVs and 12 GUVs). p-values from paired Kolmogorov-Smirnov test with 95% confidence interval. (b) Maximum intensity projection of Atto542-SspB-AuroraB before and after irradiation with 488 nm light for 15 minutes. Scalebar 10 µm.

As a first step, it was investigated if the light-induced translocation of SspB-AuroraB to iLIDg on the membrane was still working with the modified synMMS. Before the translocation was started, dark binding of SspB-AuroraB could be detected to the outer membrane of the GUVs whereas this was not clearly the case inside of the ILVs formed. This resulted in an increased R on the outside of the GUVs compared to the inside of the ILVs in the dark (Fig. 19a, black and green). Upon light-induced translocation, R for both inside ILVs and outside GUVs increased (Fig. 19a, red and blue) which was in accord with the results of the optical dimerizer system alone (5.4.2). Furthermore, it was observed that not only the plane of photo-activation showed an increased SspB-AuroraB translocation but the whole GUV was covered with translocated SspB-AuroraB (Fig. 19b).

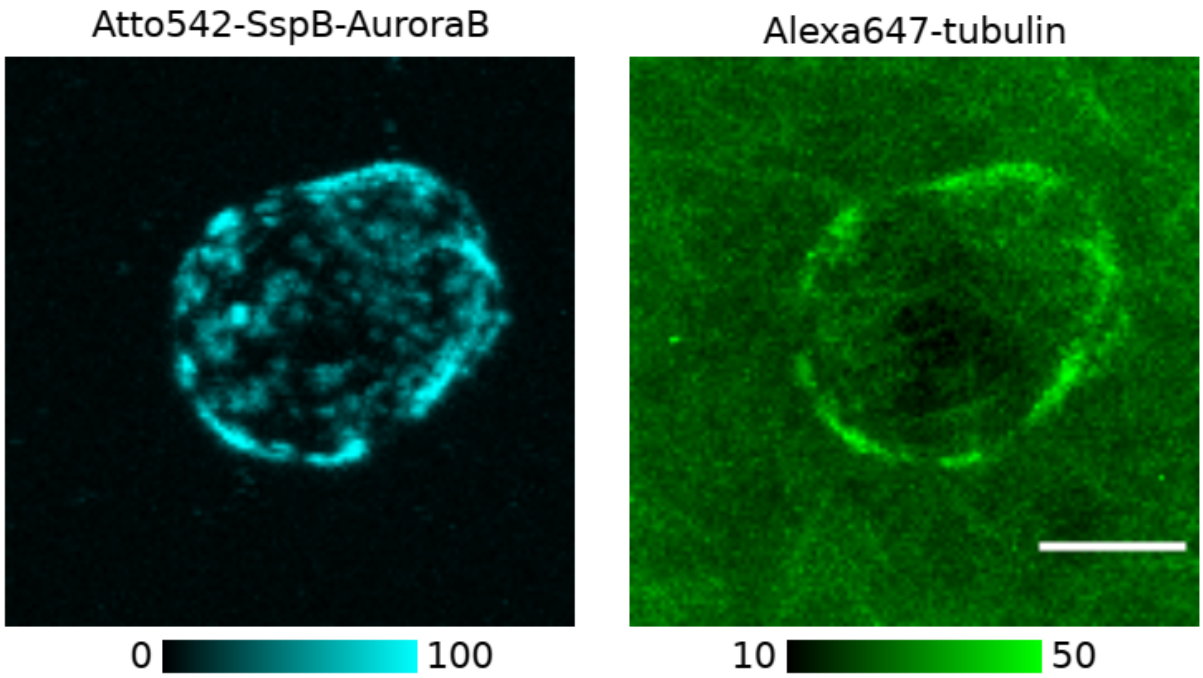

Figure 20 SspB-AuroraB as nucleation factor for tubulin outside of GUVs. Maximum intensity projection of 2 µM Atto542-SspB-AuroraB (left) and 40 µM Alexa647-tubulin (right) after 15 minutes of irradiation with 488 nm light with the full synMMS. Scalebar 5 µm.

Strikingly, upon tubulin was recruited to the membrane of the GUV with a short time delay in comparison to SspB-AuroraB (Fig. 20, left). After further observation the recruited tubulin formed a dense MT-mesh around the whole GUV (Fig. 20, right). This tubulin accumulation did not occur inside of ILVs, which points towards a concentration dependency of this effect, considering the near infinite reservoir of tubulin in the bulk surrounding the GUVs while the tubulin reservoir inside the ILVs is limited by its volume and further influenced by the depletion of tubulin into MT-structures. This effect of tubulin recruitment to the outside of the GUV was also present when stathmin was excluded from the synMMS system.

This result suggest that SspB-AuroraB acts as nucleation factor especially when in high concentrations.

5.5.2 Signal induced changes in MT-organization inside ILVs

It was further investigated if the activation of the signalling system could change the MT-organization inside of ILVs. For this, 3D stacks of GUVs with ILVs inside were taken before and after illumination with 488 nm light. ILV were imaged for 5 minutes without illumination, to observe changes in the MT-organization before light-activation. Afterwards, the system was activated for 15 minutes with 488 nm light.

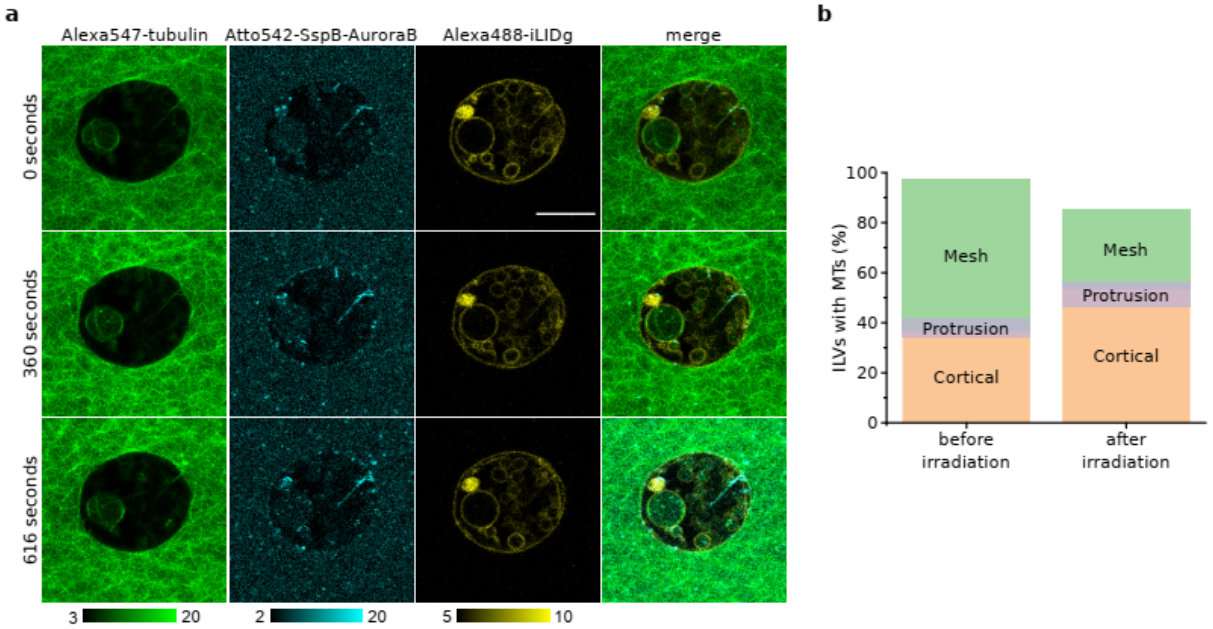

Figure 21 Global MT-organization change upon stimulation. (a) Representative CLSM images and merges of a activation series of synMMS with 40 µM Alexa647-tubulin (green), 2 µM Atto542-SspB-AuroraB (cyan) and 10 µM Alexa488-iLIDg (yellow). Scalebar 10 µm. (b) MT-formation inside ILVs with the conditions as in (a) before and after irradiation with 488 nm light for 15 minutes. Cortical MTs (orange) and MT-mesh (green) show a portion of ILVs with protrusion (purple overlay).

When observing the system over time before and during photo-activation, the MT-structures inside the ILVs displayed dynamic behaviour (Fig. 21a).

The initial MT-organization showed a cortical MT-organization in 36.6 % of ILVs, while 61 % of ILVs showed a MT-mesh (Fig. 21b, before irradiation). As for the tubulin system alone (5.3.1), the synMMS also had ILVs that formed protrusions with a total of 7.3 %, where 2.4 % originated from cortical MTs and 4.9 % from a MT-mesh, while 2.4 % of ILVs did not show any MT-structures. After the system was activated for 15 minutes, the amount of cortical MTs increased by 17.1 % to 53.7 % with 7.3 % showing a protrusion as well. On the other hand, the amount of ILVs with an MT-mesh decreased by 29.3 % to 31.7 % with 2.4 % of ILVs showing protrusions originating from them. The amount of ILVs that showed no MT-structure after the activation increase by 12.2 % to 14.6 % (Fig. 21b, after irradiation). This increase in ILVs losing MT-structures is caused by two major factors. The first main factor is the degradation of the

system over time and the second factor is photo-damage to the protein during the imaging time. The increase in cortical MTs indicates that the activation of the signalling system increases the free tubulin concentration and thereby enhances MT-growth, which leads to the elongation of existing MTs. The elongated MTs then grow beyond the boundary of the ILV, which forces the MTs either to bend along the membrane concerting a mesh to a cortical organization or forces the generation of a protrusion if the ILVs membrane is elastic enough to allow for it.

These results demonstrate that the synMMS system changes its MT-organization structure upon light activation, even with no central MTOC as described it in previous work[70]. The light induced tubulin pump in the synMMS increases MT-growth and can thereby promote the change in organization.

6. Discussion

6.1 The ehESCRT-III scission machinery as an encapsulation method

The results demonstrate the capability of the ehESCRT-III scission machinery to encapsulated a variety of synthetic cytoplasms, from simple samples with only one soluble protein like EGFP and tubulin to samples with multiple proteins and interactive networks. The encapsulation generates ILVs of the size of prokaryotic to small eukaryotic cells or organelles of higher eukaryotic cells. As indicated by other studies, for ESCRT-III homologues from yeast, the size of the generated ILVs can be influenced by the ratios used between the individual subunits of the ESCRT-III complex[107]. But rather than optimizing the concentrations of all four subunits of the ehESCRT-III machinery, the system could be possibly simplified by creating a ESCRT-III chimera, which would combine the major features of the four subunits and was already disclosed for homologues from yeast[108]. The initial membrane binding can be facilitated by the N-terminus for ehVps20, combined with the coiled coil motif of ehVps32 for homomultimerisation and spiral formation, and for recycling of the chimera the C-terminus of ehVps2 could be used. This would not only simplify the encapsulation process experimentally but further would reduce the time requirement for lengthy incubations between addition of the subunits.

The results furthermore show that the functionality of the proteins encapsulated into the ILVs is fully preserved. This was true for both soluble proteins as well as proteins that associate to the membrane via peripheral interactions. The encapsulation efficiency of soluble proteins with ~80 % was consistent with other encapsulation methods[70] and can easily be adjusted before the experiments, considering the desired protein concentration inside the ILVs.

Furthermore, it could be demonstrated, that the encapsulation of larger multi-protein complexes is possible with this method, which enables preformed complexes to pass the membrane neck into ILVs during their formation. This has the advantage that protein complexes can be preformed before the encapsulation and the assembly is not limited to times after the encapsulation reaction.

An additional feature of the encapsulation with ehESCRT-III is the ability to combine a measurement in an ILV with a simultaneous bulk control outside the GUV. This can immediately indicate if an experiment will work or has to be further adjusted.

The encapsulation also featured topology inversion from a quasi-infinite reservoir of protein and resources outside of the GUVs, which are constantly exchanged due to diffusion, to a highly resources-limited environment where no matter can be exchanged. This enables also the possibility to see differences in the behaviour of the two uncoupled systems after encapsulation.

Taken together, the ESCRT-III machinery can be utilized as a reproducible encapsulation method for a diverse set of synthetic cytoplasms and protein systems with additional features.

6.2 Encapsulation of the synthetic cytoplasm and behaviour of synMMS in bulk

With the work it could be demonstrated that synMMS, without a central MTOC reacts to a light stimulus by changing the MT-organization within ILVs. The MT-organization mainly changed from a MT-mesh towards cortical MTs, while the formation of protrusions was not exclusive to either of these two MT-organizations, but protrusions could rather originate from both states.

The results with synMMS additionally revealed that SspB-AuroraB acts as a nucleation factor for tubulin, which could especially be observed outside of the GUVs when the signalling system was activated by irradiation with 488 nm light. The light-induced signalling enhanced MTs growth close to the membrane of the GUV, forming a dense MT-mesh around the whole GUV.

Furthermore, SspB-AuroraB clusters formed on the outside of the GUVs, similar to what has been described in previous work with synMMS[70] for inside of GUVs.

In contrast to our previous work with synMMS, which suffered from the drastic loss of C2-iLID and iLIDg during the encapsulation process via cDICE, the encapsulation with the ESCRT-III machinery demonstrated, especially for iLIDg, only a 2-fold decrease in the membrane density between outside the mother GUV and inside the ILVs.

To further mimic the synMMS with a central MTOC, like centrosomes, the system could be extended with crosslinking motors in combination with specific nucleation factors to generate a central MTOC *de novo* after the encapsulation is completed[109].

The relative short life span of synMMS due to the limited reservoir of energy sources (ATP, GTP) still remains a limiting factor during measurements. With the system usually collapsing after one hour of imaging at 37 °C, this could be circumvented by including a system to generate energy, e.g. by artificial photosynthetic membranes[110].

On a different note, with an average of 4.1 ILVs formed in one GUV the system could enable the investigation of interactions between two or more proto-cells, possibly leading to new insights into recursive cell-cell communication between the proto-cells[10].

7. References

1. Damiati, S. New opportunities for creating man-made bioarchitectures utilizing microfluidics. *Biomed. Microdevices* **21**, 62 (2019).
2. Schwille, P. Bottom-up synthetic biology: engineering in a tinkerer's world. *Science* **333**, 1252–1254 (2011).
3. Way, J. C., Collins, J. J., Keasling, J. D. & Silver, P. A. Integrating biological redesign: where synthetic biology came from and where it needs to go. *Cell* **157**, 151–161 (2014).
4. Bruggeman, F. J. & Westerhoff, H. V. The nature of systems biology. *Trends Microbiol.* **15**, 45–50 (2007).
5. Ruder, W. C., Lu, T. & Collins, J. J. Synthetic biology moving into the clinic. *Science* **333**, 1248–1252 (2011).
6. Schwander, T., Schada von Borzyskowski, L., Burgener, S., Cortina, N. S. & Erb, T. J. A synthetic pathway for the fixation of carbon dioxide in vitro. *Science* **354**, 900–904 (2016).
7. Milinski, M. & Heller, R. Influence of a predator on the optimal foraging behaviour of sticklebacks (Gasterosteus aculeatus L.). *Nature* **275**, 642–644 (1978).
8. King, H., Ocko, S. & Mahadevan, L. Termite mounds harness diurnal temperature oscillations for ventilation. *Proc. Natl. Acad. Sci.* **112**, 11589–11593 (2015).
9. Yang, H. W., Collins, S. R. & Meyer, T. Locally excitable Cdc42 signals steer cells during chemotaxis. *Nat. Cell Biol.* **18**, 191–201 (2016).
10. Koseska, A. & Bastiaens, P. I. Cell signaling as a cognitive process. *EMBO J.* **36**, 568–582 (2017).
11. Milcovich, G. *et al.* Recent advances in smart biotechnology: Hydrogels and nanocarriers for tailored bioactive molecules depot. *Adv. Colloid Interface Sci.* **249**, 163–180 (2017).
12. Walde, P., Cosentino, K., Engel, H. & Stano, P. Giant vesicles: preparations and applications. *Chembiochem Eur. J. Chem. Biol.* **11**, 848–865 (2010).
13. Akbarzadeh, A. *et al.* Liposome: classification, preparation, and applications. *Nanoscale Res. Lett.* **8**, 102 (2013).
14. Lasic, D. D. & Papahadjopoulos, D. *Medical Applications of Liposomes*. (Elsevier, 1998).
15. Kahya, N. Protein-protein and protein-lipid interactions in domain-assembly: lessons from giant unilamellar vesicles. *Biochim. Biophys. Acta* **1798**, 1392–1398 (2010).
16. Mathivet, L., Cribier, S. & Devaux, P. F. Shape change and physical properties of giant phospholipid vesicles prepared in the presence of an AC electric field. *Biophys. J.* **70**, 1112–1121 (1996).
17. K. F. Pistel, T. K. Effects of salt addition on the microencapsulation of proteins using W/O/W double emulsion technique. *J. Microencapsul.* **17**, 467–483 (2000).
18. Richmond, D. L. *et al.* Forming giant vesicles with controlled membrane composition, asymmetry, and contents. *Proc. Natl. Acad. Sci. U. S. A.* **108**, 9431–9436 (2011).
19. Hurley, J. H. ESCRTs are everywhere. *EMBO J.* **34**, 2398–2407 (2015).
20. Rothman, J. H. & Stevens, T. H. Protein sorting in yeast: mutants defective in vacuole biogenesis mislocalize vacuolar proteins into the late secretory pathway. *Cell* **47**, 1041–1051 (1986).
21. Bankaitis, V. A., Johnson, L. M. & Emr, S. D. Isolation of yeast mutants defective in protein targeting to the vacuole. *Proc. Natl. Acad. Sci. U. S. A.* **83**, 9075–9079 (1986).
22. Issman-Zecharya, N. & Schuldiner, O. The PI3K class III complex promotes axon pruning by downregulating a Ptc-derived signal via endosome-lysosomal degradation. *Dev. Cell* **31**, 461–473 (2014).

23. Jimenez, A. J. *et al.* ESCRT machinery is required for plasma membrane repair. *Science* **343**, 1247136 (2014).
24. Morita, E. *et al.* ESCRT-III protein requirements for HIV-1 budding. *Cell Host Microbe* **9**, 235–242 (2011).
25. Samson, R. Y., Dobro, M. J., Jensen, G. J. & Bell, S. D. The Structure, Function and Roles of the Archaeal ESCRT Apparatus. in *Prokaryotic Cytoskeletons: Filamentous Protein Polymers Active in the Cytoplasm of Bacterial and Archaeal Cells* (eds. Löwe, J. & Amos, L. A.) 357–377 (Springer International Publishing, 2017). doi:10.1007/978-3-319-53047-5_12.
26. Hurley, J. H. & Hanson, P. I. Membrane budding and scission by the ESCRT machinery: it's all in the neck. *Nat. Rev. Mol. Cell Biol.* **11**, 556–566 (2010).
27. Bache, K. G., Raiborg, C., Mehlum, A. & Stenmark, H. STAM and Hrs are subunits of a multivalent ubiquitin-binding complex on early endosomes. *J. Biol. Chem.* **278**, 12513–12521 (2003).
28. Katzmann, D. J., Babst, M. & Emr, S. D. Ubiquitin-dependent sorting into the multivesicular body pathway requires the function of a conserved endosomal protein sorting complex, ESCRT-I. *Cell* **106**, 145–155 (2001).
29. Katzmann, D. J., Stefan, C. J., Babst, M. & Emr, S. D. Vps27 recruits ESCRT machinery to endosomes during MVB sorting. *J. Cell Biol.* **162**, 413–423 (2003).
30. Kostelansky, M. S. *et al.* Structural and functional organization of the ESCRT-I trafficking complex. *Cell* **125**, 113–126 (2006).
31. Agromayor, M. *et al.* The UBAP1 subunit of ESCRT-I interacts with ubiquitin via a SOUBA domain. *Struct. Lond. Engl. 1993* **20**, 414–428 (2012).
32. Zivony-Elboum, Y. *et al.* A founder mutation in Vps37A causes autosomal recessive complex hereditary spastic paraparesis. *J. Med. Genet.* **49**, 462–472 (2012).
33. Hierro, A. *et al.* Structure of the ESCRT-II endosomal trafficking complex. *Nature* **431**, 221–225 (2004).
34. Horii, M. *et al.* CHMP7, a novel ESCRT-III-related protein, associates with CHMP4b and functions in the endosomal sorting pathway. *Biochem. J.* **400**, 23–32 (2006).
35. Wollert, T., Wunder, C., Lippincott-Schwartz, J. & Hurley, J. H. Membrane scission by the ESCRT-III complex. *Nature* **458**, 172–177 (2009).
36. Carlton, J. G. & Martin-Serrano, J. Parallels between cytokinesis and retroviral budding: a role for the ESCRT machinery. *Science* **316**, 1908–1912 (2007).
37. Morita, E. *et al.* Human ESCRT and ALIX proteins interact with proteins of the midbody and function in cytokinesis. *EMBO J.* **26**, 4215–4227 (2007).
38. Henne, W. M., Stenmark, H. & Emr, S. D. Molecular mechanisms of the membrane sculpting ESCRT pathway. *Cold Spring Harb. Perspect. Biol.* **5**, a016766 (2013).
39. Carlson, L.-A., Shen, Q.-T., Pavlin, M. R. & Hurley, J. H. ESCRT Filaments as Spiral Springs. *Dev. Cell* **35**, 397–398 (2015).
40. Scheffer, L. L. *et al.* Mechanism of Ca^{2+}-triggered ESCRT assembly and regulation of cell membrane repair. *Nat. Commun.* **5**, 5646 (2014).
41. Babst, M., Wendland, B., Estepa, E. J. & Emr, S. D. The Vps4p AAA ATPase regulates membrane association of a Vps protein complex required for normal endosome function. *EMBO J.* **17**, 2982–2993 (1998).
42. Mierzwa, B. E. *et al.* Dynamic subunit turnover in ESCRT-III assemblies is regulated by Vps4 to mediate membrane remodelling during cytokinesis. *Nat. Cell Biol.* **19**, 787–798 (2017).
43. Dimaano, C., Jones, C. B., Hanono, A., Curtiss, M. & Babst, M. Ist1 regulates Vps4 localization and assembly. *Mol. Biol. Cell* **19**, 465–474 (2008).
44. Yu, Z., Gonciarz, M. D., Sundquist, W. I., Hill, C. P. & Jensen, G. J. Cryo-EM structure of dodecameric Vps4p and its 2:1 complex with Vta1p. *J. Mol. Biol.* **377**, 364–377

(2008).
45. Small, J. V., Stradal, T., Vignal, E. & Rottner, K. The lamellipodium: where motility begins. *Trends Cell Biol.* **12**, 112–120 (2002).
46. Conde, C. & Cáceres, A. Microtubule assembly, organization and dynamics in axons and dendrites. *Nat. Rev. Neurosci.* **10**, 319–332 (2009).
47. Verhey, K. J. & Gaertig, J. The tubulin code. *Cell Cycle Georget. Tex* **6**, 2152–2160 (2007).
48. Herrmann, H., Bär, H., Kreplak, L., Strelkov, S. V. & Aebi, U. Intermediate filaments: from cell architecture to nanomechanics. *Nat. Rev. Mol. Cell Biol.* **8**, 562–573 (2007).
49. Mostowy, S. & Cossart, P. Septins: the fourth component of the cytoskeleton. *Nat. Rev. Mol. Cell Biol.* **13**, 183–194 (2012).
50. Mostowy, S. Multiple roles of the cytoskeleton in bacterial autophagy. *PLoS Pathog.* **10**, e1004409 (2014).
51. Schmidt, W. J. Doppelbrechung der Kernspindel und Zugfasertheorie der Chromosomenbewegung. *Z. Für Zellforsch. Mikrosk. Anat. Abt B Chromosoma* **1**, 253–264 (1939).
52. Inoué, S. A method for measuring small retardations of structures in living cells. (1951) doi:10.1016/0014-4827(51)90037-7.
53. Gouveia, S. M. & Akhmanova, A. Cell and molecular biology of microtubule plus end tracking proteins: end binding proteins and their partners. *Int. Rev. Cell Mol. Biol.* **285**, 1–74 (2010).
54. Maiato, H., Sampaio, P. & Sunkel, C. E. Microtubule-associated proteins and their essential roles during mitosis. *Int. Rev. Cytol.* **241**, 53–153 (2004).
55. Hirokawa, N., Niwa, S. & Tanaka, Y. Molecular motors in neurons: transport mechanisms and roles in brain function, development, and disease. *Neuron* **68**, 610–638 (2010).
56. Sanchez, A. D. & Feldman, J. L. Microtubule-organizing centers: from the centrosome to non-centrosomal sites. *Curr. Opin. Cell Biol.* **44**, 93–101 (2017).
57. Mitchison, T. & Kirschner, M. Dynamic instability of microtubule growth. *Nature* **312**, 237–242 (1984).
58. Carlier, M. F. & Pantaloni, D. Kinetic analysis of guanosine 5'-triphosphate hydrolysis associated with tubulin polymerization. *Biochemistry* **20**, 1918–1924 (1981).
59. Wollman, R. *et al.* Efficient chromosome capture requires a bias in the 'search-and-capture' process during mitotic-spindle assembly. *Curr. Biol. CB* **15**, 828–832 (2005).
60. Akhmanova, A. & Steinmetz, M. O. Tracking the ends: a dynamic protein network controls the fate of microtubule tips. *Nat. Rev. Mol. Cell Biol.* **9**, 309–322 (2008).
61. Nogales, E. & Wang, H.-W. Structural mechanisms underlying nucleotide-dependent self-assembly of tubulin and its relatives. *Curr. Opin. Struct. Biol.* **16**, 221–229 (2006).
62. Olmsted, J. B. Microtubule-associated proteins. *Annu. Rev. Cell Biol.* **2**, 421–457 (1986).
63. Dehmelt, L. & Halpain, S. The MAP2/Tau family of microtubule-associated proteins. *Genome Biol.* **6**, 204 (2005).
64. Brouhard, G. J. *et al.* XMAP215 Is a Processive Microtubule Polymerase. *Cell* **132**, 79–88 (2008).
65. Van Damme, D. *et al.* In vivo dynamics and differential microtubule-binding activities of MAP65 proteins. *Plant Physiol.* **136**, 3956–3967 (2004).
66. Brattsand, G. *et al.* Quantitative analysis of the expression and regulation of an activation-regulated phosphoprotein (oncoprotein 18) in normal and neoplastic cells. *Leukemia* **7**, 569–579 (1993).
67. Belmont, L. D. & Mitchison, T. J. Identification of a protein that interacts with tubulin

dimers and increases the catastrophe rate of microtubules. *Cell* **84**, 623–631 (1996).
68. Curmi, P. A. *et al.* Stathmin and its phosphoprotein family: general properties, biochemical and functional interaction with tubulin. *Cell Struct. Funct.* **24**, 345–357 (1999).
69. Howell, B., Larsson, N., Gullberg, M. & Cassimeris, L. Dissociation of the tubulin-sequestering and microtubule catastrophe-promoting activities of oncoprotein 18/stathmin. *Mol. Biol. Cell* **10**, 105–118 (1999).
70. Gavriljuk, K. *et al.* A self-organized synthetic morphogenic liposome responds with shape changes to local light cues. *Nat. Commun.* **12**, 1548 (2021).
71. Gavet, O. *et al.* The stathmin phosphoprotein family: intracellular localization and effects on the microtubule network. *J. Cell Sci.* **111 (Pt 22)**, 3333–3346 (1998).
72. Charrasse, S. *et al.* The TOGp protein is a new human microtubule-associated protein homologous to the Xenopus XMAP215. *J. Cell Sci.* **111 (Pt 10)**, 1371–1383 (1998).
73. Gard, D. L., Becker, B. E. & Josh Romney, S. MAPping the eukaryotic tree of life: structure, function, and evolution of the MAP215/Dis1 family of microtubule-associated proteins. *Int. Rev. Cytol.* **239**, 179–272 (2004).
74. Roostalu, J., Cade, N. I. & Surrey, T. Complementary activities of TPX2 and chTOG constitute an efficient importin-regulated microtubule nucleation module. *Nat. Cell Biol.* **17**, 1422–1434 (2015).
75. van der Vaart, B. *et al.* Microtubule plus-end tracking proteins SLAIN1/2 and ch-TOG promote axonal development. *J. Neurosci. Off. J. Soc. Neurosci.* **32**, 14722–14728 (2012).
76. Gutiérrez-Caballero, C., Burgess, S. G., Bayliss, R. & Royle, S. J. TACC3-ch-TOG track the growing tips of microtubules independently of clathrin and Aurora-A phosphorylation. *Biol. Open* **4**, 170–179 (2015).
77. Herman, J. A., Miller, M. P. & Biggins, S. chTOG is a conserved mitotic error correction factor. *eLife* **9**, e61773.
78. Wittmann, T., Wilm, M., Karsenti, E. & Vernos, I. TPX2, A novel xenopus MAP involved in spindle pole organization. *J. Cell Biol.* **149**, 1405–1418 (2000).
79. Gruss, O. J. *et al.* Ran induces spindle assembly by reversing the inhibitory effect of importin alpha on TPX2 activity. *Cell* **104**, 83–93 (2001).
80. Petry, S., Groen, A. C., Ishihara, K., Mitchison, T. J. & Vale, R. D. Branching microtubule nucleation in Xenopus egg extracts mediated by augmin and TPX2. *Cell* **152**, 768–777 (2013).
81. Reid, T. A. *et al.* Suppression of microtubule assembly kinetics by the mitotic protein TPX2. *J. Cell Sci.* **129**, 1319–1328 (2016).
82. Boleti, H., Karsenti, E. & Vernos, I. Xklp2, a novel Xenopus centrosomal kinesin-like protein required for centrosome separation during mitosis. *Cell* **84**, 49–59 (1996).
83. Bird, A. W. & Hyman, A. A. Building a spindle of the correct length in human cells requires the interaction between TPX2 and Aurora A. *J. Cell Biol.* **182**, 289–300 (2008).
84. Schatz, C. A. *et al.* Importin alpha-regulated nucleation of microtubules by TPX2. *EMBO J.* **22**, 2060–2070 (2003).
85. Daub, H., Gevaert, K., Vandekerckhove, J., Sobel, A. & Hall, A. Rac/Cdc42 and p65PAK regulate the microtubule-destabilizing protein stathmin through phosphorylation at serine 16. *J. Biol. Chem.* **276**, 1677–1680 (2001).
86. Leung, T., Manser, E., Tan, L. & Lim, L. A novel serine/threonine kinase binding the Ras-related RhoA GTPase which translocates the kinase to peripheral membranes. *J. Biol. Chem.* **270**, 29051–29054 (1995).
87. Curmi, P. A. *et al.* The stathmin/tubulin interaction in vitro. *J. Biol. Chem.* **272**, 25029–25036 (1997).
88. Axelrod, D. & Wang, M. D. Reduction-of-dimensionality kinetics at reaction-limited cell surface receptors. *Biophys. J.* **66**, 588–600 (1994).

89. Adam, G. & Delbrück, M. Reduction of Dimensionality in Biological Diffusion Processes. in *Structural chemistry and molecular biology* vol. Vol. 198 198–215 (W. H. Freeman and Co., 1968).
90. Rangamani, P. *et al.* Decoding information in cell shape. *Cell* **154**, 1356–1369 (2013).
91. Guntas, G. *et al.* Engineering an improved light-induced dimer (iLID) for controlling the localization and activity of signaling proteins. *Proc. Natl. Acad. Sci. U. S. A.* **112**, 112–117 (2015).
92. Gadea, B. B. & Ruderman, J. V. Aurora B is required for mitotic chromatin-induced phosphorylation of Op18/Stathmin. *Proc. Natl. Acad. Sci. U. S. A.* **103**, 4493–4498 (2006).
93. Castoldi, M. & Popov, A. V. Purification of brain tubulin through two cycles of polymerization-depolymerization in a high-molarity buffer. *Protein Expr. Purif.* **32**, 83–88 (2003).
94. Hyman, A. *et al.* [39] Preparation of modified tubulins. in *Methods in Enzymology* vol. 196 478–485 (Academic Press, 1991).
95. Popp, M. W., Antos, J. M., Grotenbreg, G. M., Spooner, E. & Ploegh, H. L. Sortagging: a versatile method for protein labeling. *Nat. Chem. Biol.* **3**, 707–708 (2007).
96. Thomas, F. A., Visco, I., Petrášek, Z., Heinemann, F. & Schwille, P. Introducing a fluorescence-based standard to quantify protein partitioning into membranes. *Biochim. Biophys. Acta* **1848**, 2932–2941 (2015).
97. Thévenaz, P., Ruttimann, U. E. & Unser, M. A pyramid approach to subpixel registration based on intensity. *IEEE Trans. Image Process. Publ. IEEE Signal Process. Soc.* **7**, 27–41 (1998).
98. Ermentrout, G. B. & Edelstein-Keshet, L. Cellular automata approaches to biological modeling. *J. Theor. Biol.* **160**, 97–133 (1993).
99. Markus, M., Böhm, D. & Schmick, M. Simulation of vessel morphogenesis using cellular automata. *Math. Biosci.* **156**, 191–206 (1999).
100. Coyne, C. W. *et al.* Lipid bilayer vesicle generation using microfluidic jetting. *J. Vis. Exp. JoVE* e51510 (2014) doi:10.3791/51510.
101. Abkarian, M., Loiseau, E. & Massiera, G. Continuous droplet interface crossing encapsulation (cDICE) for high throughput monodisperse vesicle design. *Soft Matter* **7**, 4610–4614 (2011).
102. Avalos-Padilla, Y. *et al.* EhVps32 Is a Vacuole-Associated Protein Involved in Pinocytosis and Phagocytosis of Entamoeaba histolytica. *PLoS Pathog.* **11**, e1005079 (2015).
103. Avalos-Padilla, Y. *et al.* The Conserved ESCRT-III Machinery Participates in the Phagocytosis of Entamoeba histolytica. *Front. Cell. Infect. Microbiol.* **8**, 53 (2018).
104. Bajorek, M. *et al.* Structural basis for ESCRT-III protein autoinhibition. *Nat. Struct. Mol. Biol.* **16**, 754–762 (2009).
105. Carlson, L.-A. & Hurley, J. H. In vitro reconstitution of the ordered assembly of the endosomal sorting complex required for transport at membrane-bound HIV-1 Gag clusters. *Proc. Natl. Acad. Sci. U. S. A.* **109**, 16928–16933 (2012).
106. Chiaruttini, N. *et al.* Relaxation of Loaded ESCRT-III Spiral Springs Drives Membrane Deformation. *Cell* **163**, 866–879 (2015).
107. Booth, A., Marklew, C. J., Ciani, B. & Beales, P. A. In Vitro Membrane Remodeling by ESCRT is Regulated by Negative Feedback from Membrane Tension. *iScience* **15**, 173–184 (2019).
108. Marklew, C. J., Booth, A., Beales, P. A. & Ciani, B. Membrane remodelling by a lipidated endosomal sorting complex required for transport-III chimera, in vitro. *Interface Focus* **8**, 20180035 (2018).
109. Baumann, H. & Surrey, T. Motor-mediated cortical versus astral microtubule organization in lipid-monolayered droplets. *J. Biol. Chem.* **289**, 22524–22535 (2014).

110. Steinberg-Yfrach, G. *et al.* Light-driven production of ATP catalysed by F0F1-ATP synthase in an artificial photosynthetic membrane. *Nature* **392**, 479–482 (1998).

Acknowledgments

I would like to thank Prof. Dr. Philippe Bastiaens for the incredible opportunity to work on this project and the scientific guidance.

Further I would like to thank all current and past members of Department 2, for scientific and personal support and astonishing scientific discussions.
Specifically, I would like to thank Konstantin, Bruno, Farid, Manuel and Akhilesh for their involvement and help during this project and continuous help outside of the work place.
Also, I would like to thank Jana Seidel, Kirsten Michel and Hendrike Schütz for the excellent technical support in the lab and Sven Müller for his support regarding microscopy.

Additional thanks go to the works council of the Institute, which I enjoyed being a part of. And the IMPRS coordinators for their excellent support surrounding during the PhD.

And finally special thanks go to my family and friends for their never-ending support of my endeavours.